

The Upper Atmosphere of HD17156b

T.T.Koskinen, A.D.Aylward, S.Miller

*Department of Physics and Astronomy, University College London,
Gower Street, London WC1E 6BT, UK*

tommi@apl.ucl.ac.uk

ABSTRACT

HD17156b is a newly-found transiting extrasolar giant planet (EGP) that orbits its G-type host star in a highly eccentric orbit ($e \sim 0.67$) with an orbital semi-major axis of 0.16 AU. Its period, 21.2 Earth days, is the longest among the known transiting planets. The atmosphere of the planet undergoes a 27-fold variation in stellar irradiation during each orbit, making it an interesting subject for atmospheric modelling. We have used a three-dimensional model of the upper atmosphere and ionosphere for extrasolar gas giants in order to simulate the progress of HD17156b along its eccentric orbit. Here we present the results of these simulations and discuss the stability, circulation, and composition in its upper atmosphere. Contrary to the well-known transiting planet HD209458b, we find that the atmosphere of HD17156b is unlikely to escape hydrodynamically at any point along the orbit, even if the upper atmosphere is almost entirely composed of atomic hydrogen and H^+ , and infrared cooling by H_3^+ ions is negligible. The nature of the upper atmosphere is sensitive to the composition of the thermosphere, and in particular to the mixing ratio of H_2 , as the availability of H_2 regulates radiative cooling. In light of different simulations we make specific predictions about the thermosphere-ionosphere system of HD17156b that can potentially be verified by observations.

Subject headings: hydrodynamics — planetary systems — instabilities — plasmas — infrared: general

1. Introduction

HD17156b is a transiting, extrasolar giant planet (EGP) that was discovered recently by Fischer et al. (2007) as a part of the N2K program, which is a survey of metal-rich stars intended to identify short-period planets (Fischer et al. 2005). The transit was first detected

by a group of amateur astronomers (Barbieri et al. 2007), belonging to the *Transitsearch.org* network, which conducts photometric follow-up observations of known exoplanets that have been detected with the radial velocity method (Seagroves et al. 2003). Following on these initial detections, improved orbital and planetary parameters for HD17156b have recently been released by two groups, Gillon et al. (2007) and Irwin et al. (2008), both of whom performed independent transit photometry on the system with different ground-based telescopes. For this work, we have mostly adopted the parameters given in Gillon et al. (2007).

HD17156b orbits a G0 star at a distance of ~ 78 pc from Earth. Based on the observations of Fischer et al. (2007), the bolometric luminosity of the star is $2.6 L_{Sun}$ and its age is ~ 5.7 Gyr. Its effective temperature, $T_{eff} = 6079$ K, metallicity $[Fe/H] = 0.24$, radius $R_* = 1.47 R_{Sun}$, and mass, $M_* = 1.2 M_{Sun}$. Fischer et al. (2007) note that the absence of Ca II H & K line emission in the spectrum of the star indicates low chromospheric activity. They measured $S_{HK} = 0.15$ and $R'_{HK} = -5.04$, and derived a rotational period $P_{ROT} = 12.8$ days for the star. These observations have implications on the likely magnitude of the stellar XUV emissions that are an important energy source in the upper atmosphere of the planet.

HD17156b is in many ways a remarkable planet. The semi-major axis of its orbit is $a = 0.16$ AU, and the orbit is highly eccentric, with an eccentricity of $e = 0.67$. The orbital period of $P = 21.2$ days is the longest among the known transiting planets. Due to these characteristics, the planet faces a 27-fold stellar flux variation during each orbit, as it moves from ~ 0.27 AU at apastron to 0.052 AU at periastron. In addition to its curious orbit, HD17156b is unique in other ways as well. It is over three times as massive as Jupiter, but its radius is comparable to that of Jupiter. The average density of the planet is thus $\rho_p = 3.47 \rho_{Jup}$, and this makes it one of the densest gas giants known at present.

Due to the high eccentricity of its orbit, and the relatively long semi-major axis, HD17156b is not likely to be rotationally synchronised to its host star. However, the strong tidal forces between the planet and the star during periastron are likely to have driven it into ‘pseudo-synchronous’ rotation (Barbieri et al. 2007). ‘Pseudo-synchronous’ rotation implies synchronisation during periastron, but asynchronous rotation elsewhere along the orbit. The character of the orbit and the rotation of the planet around its axis make HD17156b an interesting subject for dynamical studies of its atmosphere. Irwin et al. (2008) simulated the meteorology in the photosphere of the planet by using the climate model of Langton & Laughlin (2008), and used the results to estimate the phase-dependent $8 \mu\text{m}$ infrared emissions from the planet. In this paper, we present three-dimensional simulations of the upper atmosphere and ionosphere of the planet, and investigate the stability of the atmosphere against thermal evaporation.

Absorption by atomic hydrogen in the atmosphere of another close-in EGP, HD209458b,

observed in the stellar Lyman α emission line during the transit of the planet across its host star, indicates that it is surrounded by an extended atmosphere, composed mainly of atomic hydrogen and H^+ (Vidal-Madjar et al. 2003, 2008). The observations indicate that the atmosphere is escaping hydrodynamically with a minimum mass loss rate of 10^{10} gs^{-1} . This conclusion is also supported by the tentative detection of oxygen and ionised carbon in the upper atmosphere of the planet (Vidal-Madjar et al. 2004), the detection of hot atomic hydrogen in the thermosphere (Ballester et al. 2007) and numerous modelling studies (eg. Yelle 2004, 2006; Tian et al. 2005; Garcia Munoz 2007; Erkaev et al. 2007). A recent attempt to constrain the mass loss from the planet further yielded a rate of $(1.1 \pm 0.3) \times 10^{10} \text{ gs}^{-1}$ (Schneider et al. 2007). This estimate is based on modelling the Lyman α absorption, taking into account the interaction of the exosphere with the incoming stellar wind.

While it is reasonable to suggest that the atmospheres of other close-in EGPs should undergo hydrodynamic escape as well, compelling observational evidence only exists for HD209458b. In general, the stability of the atmosphere against hydrodynamic escape depends on the conditions in the upper atmosphere and ionosphere, which are heated mainly by the absorption of stellar XUV radiation. Models of the thermosphere can thus be used to assess the overall stability of EGP atmospheres. Using a three-dimensional thermosphere-ionosphere model for extrasolar giant planets (EXOTIM), we recently published simulations of the upper atmospheres of Jupiter-type EGPs orbiting a solar-type host star at different distances (Koskinen et al. 2007a). These simulations indicate that infrared cooling from H_3^+ ions may play an important role in cooling the thermospheres of EGPs. This H_3^+ cooling effect was modelled earlier by (Yelle 2004, 2006) for HD209458b in a context of a one-dimensional non-hydrostatic model. Our calculations extended this effect to three dimensions and a wider sample of orbital distances. We also identified a sharp stability limit for the atmosphere of a Jupiter-type exoplanet orbiting the Sun at $\sim 0.15 \text{ AU}$ (Koskinen et al. 2007b). Within this limit molecular hydrogen breaks down in the upper atmosphere due to thermal dissociation, the atmosphere expands, and begins to escape hydrodynamically. Outside the limit, the thermosphere is effectively cooled by H_3^+ , and the atmosphere does not undergo fast hydrodynamic escape.

In this context, HD17156b is an interesting subject for similar modelling studies. During periastron, the atmosphere of the planet should absorb enough XUV radiation from the star to undergo hydrodynamic escape, whereas at apastron distances we would not expect this to be the case. Of course, this kind of reasoning is oversimplistic. The planet may not spend long enough near periastron for the atmosphere to heat up, or it may not have enough time to cool down during apastron. As a result, the atmosphere may be stable throughout the whole orbit, or it may escape hydrodynamically at every point. Also, HD17156b is much heavier than Jupiter (that we used as a template in our earlier work). Consequently, the

scale heights in the atmosphere are shorter, and due to higher gravity, particles need more thermal kinetic energy to escape the atmosphere. Higher gravity may thus help to maintain stability even at close-in distances during periastron.

In order to make predictions about the upper atmosphere, ionosphere, and potential infrared emissions, we have modified EXOTIM to simulate the progress of HD17156b along its eccentric orbit. The details of the new model are discussed in Section 2. Section 3 describes the results of the modelling along with some caveats, and Section 4 discusses the implications of our results in the context of potential observations and relates them to earlier work on this subject.

2. The Model

2.1. Basic equations

The model solves the three-dimensional Navier-Stokes equations of continuity, momentum and energy by explicit time-integration, assuming that the thermosphere is dominated by H_2 , He and H and that it is in hydrostatic equilibrium throughout. The basic equations are solved on a non-inertial Eulerian, corotating spherical grid, using spherical pressure coordinates. The details of the equations, and the model in general, are described extensively in Koskinen et al. (2007a) and are thus not repeated here. However, since the publication of that paper, we have added a number of improvements and modifications to the model, which are introduced below. Some of these changes were also described in the Supplementary Information of Koskinen et al. (2007b). It should be noted that the resulting equations resemble the primitive equations of meteorology, with the exception that they include terms due to molecular diffusion, which are important in the rare gas of the upper atmosphere. Also, our equations fully include the curvature terms arising from spherical coordinates.

As before, we solve for the horizontal winds from the momentum equations, accounting for advection, geopotential gradients, the Coriolis force and viscosity due to molecular diffusion. Once the horizontal velocities are known, we solve for the vertical velocities from the continuity equation. The temperatures are solved from the energy equation, which accounts for the advection of energy around the atmosphere by circulation, the absorption of stellar X-rays and EUV (XUV) radiation, infrared cooling (by H_3^+), heating and cooling due to adiabatic contraction and expansion, vertical and horizontal conduction of heat and viscous heating. The basic equations of motion are coupled to continuity equations for neutral mass fractions that account for vertical and horizontal advection, vertical diffusion and neutral chemistry. The numerical solution is based on finite-difference approximations of spatial

derivatives and forward-time integration. This scheme is prone to numerical instabilities, which we filter out by using the two-step smoothing element described by Shapiro (1970). This element has been adapted for spherical geometry and vector equations, where appropriate. We only apply smoothing in the horizontal direction, and use the filter every 144 s of runtime on temperatures and winds, and every 36 s of runtime on mass mixing ratios of the neutral species. Generally, the timestep in the simulations varies between 1-2 s.

2.2. Composition

As an improvement on the previous model, we have updated the photochemistry and calculated new values for the absorption cross sections of H₂, He and H throughout the XUV spectrum. The new reaction list with appropriate references is shown in Table 1. Instead of using coefficients of heat conduction and molecular diffusion for atomic hydrogen given by Achilleos et al. (1998), we have adopted values from Banks & Kockarts (1973). The coefficients for other species are as before. We note that the changes do not affect the results presented in Koskinen et al. (2007a) significantly.

We determine ion densities by calculating photoionisation by stellar XUV radiation, and model the subsequent photochemistry by using the reactions listed in Table 1 and assuming photochemical equilibrium. In doing so, we effectively ignore ion transport, thus assuming that ion lifetimes are short. Also, we calculate the overall neutral density from the ideal gas law, assuming that photoionisation has negligible *direct* impact on neutral mass fractions. This assumption is valid as long as ion densities are much smaller than neutral densities.

In general, the number density of ion species i , n_i is given by:

$$\frac{dn_i}{dt} = P_i + L_i n_i \quad (1)$$

where P_i and L_i are the production and loss rates of species i , respectively. For a tidally locked planet in photochemical equilibrium, we have $P_i + L_i n_i = 0$, and the resulting series of non-linear, simultaneous equations can be solved by using Newton-Raphson iteration (Koskinen et al. 2007a; Press et al. 1992). However, if the planet rotates asynchronously, the rate of change in density n_i is not zero in the Eulerian, corotating frame. For such planets, our previous model used a crude time-integration technique:

$$n_i(t + \delta t) = n(t) + (P_i + L_i n_i)\delta t \quad (2)$$

This method is unstable for short ion lifetimes, which are typical for H₂⁺, H₃⁺, and He⁺. In

general, it requires unrealistically short time steps, and it also forced us to assume that all H_2^+ is immediately turned into H_3^+ . Thus we were unable to model the H_2^+ densities self-consistently for asynchronously rotating planets. Clearly, such a limitation would have been unacceptable for planet in ‘pseudo-synchronous’ rotation such as HD17156b.

Equation (1) can be integrated with respect to time by using the method of integrating factors, and thus we used an improved time-integration formula:

$$n_i(t + \delta t) = \frac{P_i}{L_i}(1 - e^{-L_i\delta t}) + n_i(t)e^{-L_i\delta t} \quad (3)$$

As long as the time step δt is kept reasonably short, this method produces accurate ion densities for asynchronously rotating atmospheres in photochemical equilibrium. It also allows us to fully include H_2^+ in the calculations.

2.3. XUV Heating

Previously the model included stellar radiation between 5.0 and 105 nm. We have extended this range to cover X-rays, and now include radiation from 0.1 to 105 nm. We note that for XUV emissions typical of the current Sun, the inclusion of X-rays in our input has almost no impact on the properties of the thermosphere compared to models that do not include X-rays. Some authors have proposed that X-rays have a significant impact on the atmospheres of EGPs orbiting young G stars (eg. Cecchi-Pestellini et al. 2006; Penz et al. 2008), and this may well be the case because a more significant fraction of the total XUV flux from young stars is in X-rays than from mature solar-type stars (Ribas et al. 2005). However, it is not true for EGPs orbiting mature main sequence G stars such as the Sun.

We assume that the XUV flux from HD17156b is roughly similar to solar flux, and use solar maximum fluxes from the SOLAR2000 model (Tobiska et al. 2000) in these simulations. This assumption is not likely to be accurate, and considerably variation in the XUV flux is possible. Unfortunately, there are no observations or models of the XUV emissions from HD17156. The intensity of the emissions is related to the strength of the stellar magnetic dynamo, which depends on the rotation rate of the star (Ribas et al. 2005). The period of rotation for HD17156 is half that of the Sun, so the XUV flux could be slightly higher, but this is speculative. In the absence of better estimates, we have little choice but to adopt solar emissions for the time being. Despite this uncertainty, the models will still help us to develop an understanding of the relative dynamics and structure in the thermosphere, and perhaps the predictions can be tested with future observations.

It should be noted here that we did not perform detailed energetic calculations to work out the heating rate due to the absorption of stellar XUV energy. Instead, we assumed that 50 % of the absorbed energy is thermalised in a H_2 -dominated atmosphere. This is consistent with calculations performed by Waite et al. (1983) for Jupiter’s upper atmosphere that account for all other energetic processes apart from H_3^+ cooling. Following Yelle (2004), we assumed a 10 % heating efficiency in those layers of the thermosphere that are dominated by atomic hydrogen.

2.4. Infrared Cooling

The only infrared cooling source included in our model is due to H_3^+ emissions. We assume that the upper atmosphere is optically thin in the infrared and ignore radiative transfer. Thus any emitted infrared radiation escapes directly to space or to the lower atmosphere, and in both cases contributes to the cooling of the thermosphere. We neglect the possible presence of hydrocarbons or carbon monoxide near the lower boundary of the model that may in reality complicate this picture.

In order to calculate the total emission rate in local thermodynamic equilibrium (LTE), we employ the complete H_3^+ line list published by Neale et al. (1995). However, the frequency of intermolecular collisions in the upper atmospheres of gas giants is generally too low to maintain LTE conditions. Previously, we estimated non-LTE emission rates by multiplying the LTE rates by a pressure-dependent correction factor, which was derived experimentally by fitting to *Galileo* observations of Jupiter’s thermosphere (Koskinen et al. 2007a). As an improvement, we now base the correction factor on detailed balance calculations.

It would be computationally impossible to perform detailed balance calculations for over three million line transitions included in the H_3^+ line list, at every grid point in the model, and during each time step. Instead, we have singled out prominent vibrational transitions included in an earlier line list of Dinelli et al. (1992) that account for most of the LTE infrared emissions. We determined both the LTE and non-LTE emission rates for these transitions, adopting detailed balance calculations for the non-LTE emissions, and calculated the ratio of the total non-LTE rates to LTE rates for a simple grid of temperatures and densities that encompasses the likely values within the model. We then created a table of non-LTE/LTE ratios for different temperatures and densities. As the model runs, it interpolates from this table bilinearly in order to work out the non-LTE/LTE ratio for each grid point. The final emission rate is worked out by multiplying the total LTE emission rate, evaluated by using a fourth-order fitted polynomial to the values given by Neale et al. (1995), by this ratio. This method essentially assumes that the non-LTE correction is the same for the complete line list

as it is for the reduced line list of Dinelli et al. (1992). The resulting ratios are listed for the substellar point of a typical model run, together with temperatures and pressures, in Table 2. For comparison, experimental correction factors given by equation (15) of Koskinen et al. (2007a) are also shown.

2.5. The Orbit

Figure 1 is a crude illustration of the orbit of HD17156b, which also shows the orientation of the orbit with respect to an observer on Earth. The transit is offset clockwise from periastron by 31.1 degrees. The inclination of the orbit is $i = 85.4$ degrees (Gillon et al. 2007), although this figure has been revised to 86.5 degrees by Irwin et al. (2008). It is not clear if a secondary eclipse exists. Gillon et al. (2007) suggest that it should be a partial grazing eclipse, but Irwin et al. (2008) ascribe only a 9.2 % chance for this to be case. The probability of a full secondary eclipse is even lower at 6.9 %. In case secondary eclipse does occur, the angular separation between the antitransit and periastron is 148.9 degrees.

Simulating the planet’s progress on its eccentric orbit is done by varying the irradiation conditions continuously as the planet moves along the orbit. For this purpose, we need to work out the true anomaly, which is the angular distance of the planet from periastron, and the distance of the planet from the star as a function of time. Also, as we assume that the planet is locked in ‘pseudo-synchronous’ rotation around its axis, we need to account for the planet’s spin by varying the position of the star in the corotating frame of the planet.

The ‘pseudo-synchronous’ spin angular velocity is given by (Hut 1981):

$$\Omega_{sp} = \frac{1 + (15/2)e^2 + (45/8)e^4 + (5/16)e^6}{[1 + 3e^2 + (3/8)e^4](1 - e^2)^{3/2}} \bar{\Omega} \quad (4)$$

where e is the eccentricity, and $\bar{\Omega}$ is the mean orbital angular velocity. Using $e \sim 0.67$ yields $\Omega_{sp} \sim 5.6 \bar{\Omega}$. This means that during one full orbit the planet spins around its axis 4.6 times in the star’s frame of reference.

In terms of the orbital angular velocity during periastron, Ω_p , the ‘pseudo-synchronous’ spin angular velocity can be expressed as:

$$\Omega_{sp} = \frac{1 + (15/2)e^2 + (45/8)e^4 + (5/16)e^6}{[1 + 3e^2 + (3/8)e^4](1 + e)^2} \Omega_p \quad (5)$$

Again using $e \sim 0.67$ yields $\Omega_{sp} \sim 0.818 \Omega_p$. In other words, during periastron the planet’s spin is slower than the orbital angular velocity, and while passing the periastron the planet

should therefore revolve ‘backwards’ with respect to the star compared to normal, faster spin at other parts of the orbit. This behaviour is a curious feature of ‘pseudo-synchronisation’ and it causes a peculiar jitter in the position of the star in the planet’s sky near periastron.

The orbital mean anomaly is given by:

$$M(t) = \frac{2\pi}{P}(t - T) \quad (6)$$

where P is the orbital period and T is the time of periastron. This is simply the angular distance traversed by the planet in time $(t - T)$ if the orbit was circular. Mean anomaly can be related to the eccentric anomaly by using Kepler’s second law, which states that the radius vector from the host star to the planet sweeps out equal areas in equal time, and the geometric properties of an ellipse. The relation between the mean and eccentric anomalies is given by Kepler’s equation:

$$M = E - e \sin(E) \quad (7)$$

where E is the eccentric anomaly. By using the general equation of an ellipse and geometric relations, it is straightforward to show that the true anomaly, θ , is related to the eccentric anomaly by:

$$\cos(\theta) = \frac{\cos(E) - e}{1 - e \cos(E)} \quad (8)$$

Once true anomaly is known, it is easy to solve for the orbital distance as a function of time by using:

$$d(t) = \frac{a(1 - e^2)}{1 + e \cos[\theta(t)]} \quad (9)$$

where a is the semi-major axis of the orbit.

Kepler’s equation (7) is a transcendental equation, which cannot be solved analytically. Fortunately, it can be solved easily by using Newton-Raphson iteration. For this purpose, the equation is first written as:

$$f(E) = E - e \sin E - M = 0$$

If the initial guess at the solution is given by E_g , then the progressive corrections to this solution are given by:

$$E = E_g - \frac{f(E_g)}{f'(E_g)}$$

where $f'(E_g)$ is the differential of f with respect to E . The iteration proceeds until an acceptable level of convergence is achieved. In general, the solution to Kepler’s equation converges very quickly and only a few iterations are required. Analytically, it can be shown that for $e < 0.99$ and an initial guess of π , convergence is guaranteed.

The change in the local hour angle in time δt is given by the numerical difference of the spin angular velocity and orbital angular velocity multiplied by δt :

$$\delta H_a = [\Omega_{sp} - \Omega(\theta)]\delta t \tag{10}$$

where $\Omega(\theta)$ is the orbital angular velocity, which depends on the true anomaly of the planet’s position. Note that near periastron, where $\Omega(\theta)$ is faster than Ω_{sp} , δH_a can become negative.

The above suite of equations allows us to model the stellar irradiation on the atmosphere at every point along the orbit. During every time step the model calculates a new value for the mean anomaly. This value is then converted into true anomaly by using equations (7) and (8). The distance to the host star is then calculated from equation (9) and this distance is used to obtain the dilution factor for the stellar XUV flux. Equation (10) is used to calculate the position of the star in the planet’s sky. Given that this procedure is repeated every timestep, it proceeds surprisingly swiftly and does not add much to overall computation time.

Figure 2 shows the orbital true anomaly versus time for the orbit of HD17156b, Figure 3 shows the orbital distance versus true anomaly and Figure 4 shows how the hour angle develops during one orbit. All simulations start from apastron, with $\theta = 180^\circ$, and the local zenith for the hour angle calculation is set initially at the substellar point. The plots illustrate that the orbital solution is working as it should and that it makes physical sense. Also, they demonstrate the fact that the orbital angular velocity is faster during periastron, implying that the planet spends most of the time completing the ‘far-side’ of the orbit.

2.6. Boundary Conditions and Planetary Parameters

We used planetary and orbital parameters that are listed in Table 3 together with the other input parameters for the simulations. We used parameters originally released by Gillon et al. (2007) in their preprint. These parameters have been subsequently revised, and

they also differ from those released by Irwin et al. (2008). However, given all the uncertainties in the model, and the uncertainties in the published parameters, the differences are not likely to be particularly important. The numerical solution is evaluated on a grid of 36 evenly spaced longitude points, 31 evenly spaced latitude points, and 28 pressure levels ranging from 2 μ bar to 0.04 nbar with a uniform spacing of 0.4 scale heights. The calculations do not extend to the poles and instead, the field variable values are interpolated over to the polar latitude circles (31,30,1,2). We assume that the thickness of the lower atmosphere is entirely negligible compared to the radius of the planet, and thus place the zero-altitude reference point at our lower boundary at 2 μ bar.

We assume that the lower boundary temperature is constant at $T_0 = 520$ K. This is close to the equilibrium temperature of a gas giant with a Bond albedo equal to 0.3 under solar irradiation near the apastron of HD17156b’s orbit. Using a constant lower boundary temperature for a planet like HD17156b may not be realistic as this temperature is likely to vary along the orbit. Unfortunately it is not clear how the temperature varies at the 2 μ bar level as the irradiation level changes. In order to avoid speculation we have chosen to use a constant lower boundary temperature for our reference models. However, as the effect on our model could be significant, we also produced simulations where we varied the lower boundary temperature. The results are discussed in Section 3.5.

The initial composition comes from a model of Jupiter’s auroral region (Grodent et al. 2001) that effectively fixes the mixing ratios of the neutral species at the lower boundary of the model. The lower boundary composition for a planet like HD17156b is highly uncertain. It is not clear if the dominant carbon-bearing molecule in the lower atmosphere should be CO or CH₄, and there are no constraints on the mixing ratios of heavier molecules in general. Thus we have chosen not to speculate on hydrocarbon or oxygen photochemistry, and instead assumed that the mixing ratios of heavier molecules in the thermosphere are negligible. This assumption is not as crude as it may initially appear, because due to molecular diffusion the mixing ratios of molecules heavier than He should be very small inside our pressure range.

The mixing ratios of H and He near our lower boundary are also uncertain, which is why our first instinct was to use jovian values ($\sim 2 \times 10^{-4}$ for H, and 0.056 for He). However, these values may well be inappropriate for a planet that is so different from Jupiter as HD17156b. For instance, atomic hydrogen in the upper atmosphere is created as a by-product of the complex oxygen and hydrocarbon photochemistry, which is powered by stellar UV radiation, and is expected to be taking place in the stratosphere-mesosphere region of close-in gas giants. Calculations of Liang et al. (2003), based on such photochemistry, demonstrate that the mixing ratio of atomic hydrogen near the μ bar level could be around 1 % for a close-in giant like HD209458b (with $a = 0.045$ AU). They indicate that for a variety of chemistries,

the production of atomic hydrogen is mainly limited by the strength of the UV flux, which varies 27-fold for HD17156b. Based on these arguments, we expect the mixing ratio of atomic hydrogen to be less than 1 % for HD17156b at the μ bar level because most of the time the planet is farther from the host star than HD209458b, and thus it should receive less UV radiation.

While our model is not sensitive to small variations in the mixing ratio of He at the lower boundary, the amount of atomic hydrogen could be crucial because it regulates the availability of H₂ and thus limits the formation of H₃⁺. In order to examine the effect of changing the lower boundary mixing ratio of atomic hydrogen, we have generated both Jupiter-type models and models where the mixing ratio of atomic hydrogen was raised to 1 % at the lower boundary at the expense of the mixing ratio of H₂.

For all of our simulations, we assume zero winds at the lower boundary. This point was extensively discussed in Koskinen et al. (2007a), where we also demonstrated that the inclusion of winds and temperature variations at the lower boundary does not affect the conditions in the upper atmosphere significantly. This insensitivity is due to the very strong forcing by the stellar XUV radiation in the middle-to upper thermosphere. As an upper boundary condition, we assume that vertical gradients reduce to zero in the two uppermost layers, vertical winds vanish at the upper boundary, and that the neutral species are in diffusive equilibrium in the two uppermost levels.

3. Results

3.1. Evaporation of the Atmosphere

The stability of the atmosphere against thermally driven hydrodynamic escape is determined at the exobase, which is defined as the altitude where an escaping particle undergoes approximately one collision within one atmospheric scale height. A handy measure of stability is the thermal escape parameter, given by Hunten (1973):

$$\lambda = \frac{GM_p m}{kT_c z_c} = \left(\frac{v_{esc}}{u}\right)^2 \quad (11)$$

where m is the mass of the escaping constituent, k is Boltzmann’s constant, T_c is the temperature at the critical level (exobase), and z_c is the altitude of the critical level. This is basically the square of the ratio of the escape velocity to the most probable thermal velocity, u , at the exobase. Once the thermal escape parameter becomes less than about 1.5 for H or less than about 3.0 for H₂, the thermal kinetic energy at the critical level becomes greater

than the gravitational potential energy and the atmosphere begins to escape hydrodynamically. If $\lambda > 3$, Jeans escape dominates. Of course, the transition between Jeans escape and hydrodynamic escape is not abrupt, and some overlap is to be expected for low values of λ . However, at $\lambda > 30$, even Jeans escape is fairly insignificant.

The escape velocity from HD17156b is 108 km s^{-1} , which compares to about 60 km s^{-1} for Jupiter. Thus the temperature in the upper atmosphere of HD17156b must be significantly higher for hydrodynamic escape to take place than what is required for a Jupiter-like planet. Figure 5 shows the globally averaged temperatures for HD17156b at the upper boundary of the model versus orbital true anomaly (starting from -180° at apastron). The results are shown for two types of simulations, one with lower boundary mixing ratios from Grodent et al. (2001) (Exo-1) and one with the mixing ratio of atomic hydrogen fixed at 1 % at the lower boundary (Exo-2).

For Exo-1, the exobase temperature is around 2,000 K at apastron, and it rises to over 3,000 K at periastron. The temperature peaks around periastron and reaches a minimum near apastron. The temperature difference at apastron between successive orbits is ~ 0 K, indicating that the model repeats the same behaviour during each orbit and is therefore in a kind of steady state. Remarkably, this steady state establishes itself after only three simulated orbits. The upper thermosphere is dominated by molecular hydrogen, and the thermal escape parameter varies between 690 during apastron and 410 during periastron, rendering the atmosphere stable throughout the whole orbit and even Jeans escape negligible. As expected, the thermosphere is relatively thin, with the upper boundary altitude ranging from 840 km during apastron to 1,100 km during periastron.

For Exo-2, the exobase temperatures are considerably higher, over 10,000 K throughout the orbit. The minimum temperature is around 15,000 K, reached at $\theta = -145^\circ$, and the maximum temperature is 34,000 K, reached after the periastron at $\theta = 76^\circ$. Atomic hydrogen and H^+ are virtually the only species in the upper thermosphere, and between the minimum and maximum temperature regions the thermal escape parameter ranges from 40 to 15, respectively. This implies that near periastron, Jeans escape could be significant and even some bulk flows are possible. However, according to the criteria based on the thermal escape parameter, the atmosphere should not undergo fast hydrodynamic escape at any point along the orbit. The upper boundary altitude ranges from 13,100 km ($1.2 R_p$) near the temperature minimum to 27,300 km ($1.4 R_p$) near the temperature maximum. The mass loss rate from Exo-2, based on thermal Jeans escape, peaks around 10^6 g s^{-1} at around $\theta = 76^\circ$. However, this mass loss rate is not sustained throughout the orbit, and instead it drops to less than 10^{-2} g s^{-1} around apastron.

The temperature variation between successive apastron passes for Exo-2 is ~ 130 K after

fifteen simulated orbits. This means that the simulations have not reached exact steady state, although it is reasonable to assume that they are near steady state. 130 K is not a particularly significant figure compared to the temperature of the upper boundary (over 15,000 K), and the difference gets smaller during each orbit. Computational constraints mean that we cannot run the Exo-2 simulation to exact steady state within a reasonable time period, and thus it is possible that the model keeps heating up slowly during each orbit until it reaches conditions that would lead to hydrodynamic escape. Given the rather swift passage through the periastron, however, we think that this is unlikely.

The drastic difference in the thermal characteristics of the two simulations of HD17156b, Exo-1 and Exo-2, arises from the differences in the composition of the thermosphere. Figure 6 shows the substellar mixing ratios of atomic hydrogen during apastron for the two simulations. For Exo-1, the mixing ratio of atomic hydrogen is relatively low at all levels, rising to about 6 % near the exobase. At the upper boundary, the maximum mixing ratio is about 10 % near the dawn terminator whereas the minimum is about 5.5 % near the dusk terminator. For Exo-2, atomic hydrogen becomes the dominant species between 1 and 0.1 μbar (altitude of 50-300 km). Above that level, atomic hydrogen and H^+ are virtually the only species in the thermosphere. This is because, initially, the higher mixing ratio of atomic hydrogen at the lower boundary in the Exo-2 simulation leads to a reduction in the atomic hydrogen concentration of the thermosphere through molecular diffusion. This limits the formation of H_3^+ , which reduces the significance of radiative cooling compared to the Exo-1 simulation. As a result, the temperatures become high enough to dissociate molecular hydrogen thermally, and this process quickly converts most of the upper atmosphere into atomic hydrogen that is subsequently ionised by the intense XUV radiation. It should be noted, though, that for HD17156b the transition region between the H_2 and H atmospheres is located deeper in the thermosphere than it would be for a Jupiter-type planet or HD209458b with similar lower boundary conditions because of the higher gravity on HD17156b.

Figure 7 contrasts the apastron H_3^+ densities and infrared cooling rates at the substellar points of Exo-1 and Exo-2. The substellar column densities of H_3^+ in the two models are $3.2 \times 10^{16} \text{ m}^{-2}$ and $5.0 \times 10^{14} \text{ m}^{-2}$, respectively, and in Exo-2 H_3^+ virtually disappears at pressures lower than 0.6 μbar (above 150 km). This difference in H_3^+ densities makes itself evident in the infrared cooling rates, that are prominent for Exo-1 but negligible for Exo-2. Contrasting the total infrared cooling rates to the total XUV heating rate allows us to estimate global cooling functions for the models. Depending on the orbital positions, the cooling function for Exo-1 is 72-91 % while for Exo-2 it is merely 0.1-0.24 %. The cooling function thus depends on the composition and photochemistry of the models, and the degree to which H_2 is dissociated thermally.

It is unfortunate that the conditions in the thermosphere depend on the lower boundary composition, as the mixing ratios there are difficult to constrain. On the other hand, this feature opens up interesting new avenues for observations. For instance, an observation of H Lyman α absorption during transit could be used to constrain the properties of the upper atmosphere of HD17156b in the same way as the detection of the extended hydrogen cloud around HD209458b (Vidal-Madjar et al. 2003) has allowed for the characterisation of that planet’s atmosphere. We predict that for the upper atmosphere of HD17156b to be dominated by atomic hydrogen, it should extend to more than $1.4 R_p$ during transit near periastron. If an extended hydrogen atmosphere is not detected, then infrared cooling must be taking place and the thermosphere is dominated by H_2 . Thus, even if H_3^+ emissions are too faint to be detected directly, we could infer their existence indirectly and also constrain the mixing ratios of H and H_2 in the lower atmosphere.

3.2. Circulation

Figure 8 shows the temperature and circulation at the upper boundary of Exo-1 at four different orbital positions: during apastron, a quarter orbit after apastron ($\theta = -153^\circ$), during periastron, and a quarter orbit after periastron ($\theta = 153^\circ$). If secondary eclipse takes place, the fourth orbital position we have considered here is near (although not exactly at) the longitude of the antitransit, whereas the periastron models are a fairly good representation of the transit conditions.

At all four orbital positions, the dayside is clearly warmer than the night side. At apastron, the dayside temperature is 2,200-2,300 K, and the temperature peaks at the equator near dawn. The night side temperature, with a minimum close to the dawn terminator, is 1,650-1,750 K. The diurnal temperature difference is thus 500-600 K. The horizontal winds originate in the dayside, and blow across the terminator to the night side. In the night side, the Coriolis force and the geopotential gradients drive the eastward wind towards the equator, into a stream that flows across the antistellar point and faces the westward wind from the dayside near the dawn terminator. Also in the night side, there are two high-latitude vortices that direct the easterly wind from the dayside into the westerly equatorial jet. The maximum zonal wind speed is 1.1-1.3 kms^{-1} at high latitudes. Convection is directed upwards in the dayside, accompanied with adiabatic expansion of the atmosphere, and downwards in the night side, accompanied with adiabatic contraction of the atmosphere. The maximum vertical flow speed is only a few ms^{-1} . The thermal escape parameter for the average atmosphere at the upper boundary is 689, indicating negligible thermal evaporation. An escaping particle undergoes approximately 5 collisions within one scale height above the

upper boundary, implying that the 0.04 nbar level is slightly below the exobase.

At $\theta = -153$ degrees the distance of the planet from the star is 0.22 AU. The upper boundary temperature and wind pattern is qualitatively identical to the apastron model. However, with added heating, the dayside temperatures are higher, at 2,300-2,450 K. The night side temperature is 1,650-1,850 K, implying a diurnal temperature difference of 600-700 K. The maximum zonal wind speed is also slightly higher at 1.3-1.6 kms^{-1} . The thermal escape parameter is 659, indicating that thermal evaporation is insignificant.

At periastron, where the orbital distance is 0.052 AU, the near-synchronisation of the planet's spin leads to a more pronounced diurnal temperature difference. Between $\theta = -90^\circ$ and $\theta = 90^\circ$, only one hemisphere of the planet is exposed to stellar irradiation. The dayside temperature during periastron is around 4,350 K, while the night side temperature is around 2,200 K. Thus the diurnal temperature difference is over 2,000 K. Large-scale circulation is qualitatively similar to other orbital positions, but the winds are faster, with maximum speeds of 2.6-2.8 kms^{-1} . Vertical advection is also more rigorous, and the maximum vertical wind speed is 8-15 ms^{-1} . However, despite the added heating, the thermal escape parameter is 411, and evaporation is still slow. The enhanced XUV heating is balanced by effective H_3^+ cooling, and before the thermosphere has time to heat up significantly, the planet moves away from periastron. At $\theta = 153^\circ$, the upper boundary is almost identical to the $\theta = -153^\circ$ model. There are some very slight differences between these models, but those are mostly limited to the lower thermosphere.

Deeper in the thermosphere, the situation is different. Figure 9 shows the temperature and circulation near 55 nbar (altitude of 250-300 km) for Exo-1 at the same orbital positions as above. In all cases, the temperature is nearly uniform. With the exception of periastron, the circulation is characterised by a broad eastward, circumplanetary jet. During apastron, the temperature varies between 1,530 and 1,580 K, and the equator is everywhere slightly warmer than its surroundings, with temperature peaking in the night side. The wind speed in the equatorial jet ranges from 160 to over 220 ms^{-1} . Cyclonic polar vortices circle around the minimum temperature regions near the poles. In general, the circulation in the lower thermosphere is characteristic of Coriolis-driven dynamics, that smoothes out diurnal temperature variations.

At $\theta = -153^\circ$, the temperature varies between 1,540 and 1,610 K. The equator is still warmer than its surroundings, and there are two temperature peaks, one near the substellar point and one in the night side. The temperature minima are again located near the poles near the dawn terminator, and the cyclonic polar vortices are centred on those. In the equatorial jet, the wind speed ranges from 100 to 220 ms^{-1} .

During periastron the horizontal temperature variations are more pronounced, with the temperature ranging from 1,840 to 2,020 K, but the details of the temperature distribution are confusing. The warm substellar region is surrounded by a cooler ring along the terminator, but the night side is almost as warm as the dayside. The winds diverge from the substellar point, blowing towards the night side. An eastward jet develops in the night side, but it encounters the easterly wind at dawn, and cannot encircle the planet at this pressure level. The two high-latitude vortices direct easterly flows into the equatorial jet. The maximum wind speed is around 800 ms^{-1} . The circulation is qualitatively similar to the topside circulation, and this must be a consequence of the near-synchronisation during periastron.

At $\theta = 153^\circ$, the temperature ranges from 1,580 to 1,660 K. Overall, the lower thermosphere is slightly warmer than it was at the symmetric position at $\theta = -153^\circ$, and it is in the process of cooling down after the periastron passage. The circulation is again characterised by the circumplanetary jet and the polar vortices. The wind speed in the equatorial jet ranges from 100 to 400 ms^{-1} .

For comparison, Figure 10 shows the temperature and circulation at the upper boundary of Exo-2 for the same orbital positions. The horizontal uniformity of the temperature in these simulations is remarkable, and the wind speeds are very slow. During apastron, the dayside temperature is 17,620-17,630 K, while the night side temperature is around 17,530 K. Thus the diurnal temperature difference is only of the order of 100 K. The winds blow from the dayside to the night side, and in the night side some of the eastward flow is directed into an equatorial jet that faces the easterly wind from the dayside near dawn. High-latitude vortices turn some of the easterly flow around, and direct it into the equatorial jet. In the dayside, the temperature peak is shifted slightly eastward from the substellar point by circulation and rotation. The winds are slow, with a maximum speed around 200 ms^{-1} . An escaping particle suffers ~ 14 collisions within one scale height at the upper boundary, indicating that the 0.04 nbar level is located below the exobase. However, the P-T profile is isothermal at pressures lower than ~ 0.7 nbar, and thus the temperature at the critical level should be the same as at our upper boundary. The thermal escape parameter at this boundary is 33, and the mass loss rate based on Jeans escape is $\sim 10^{-2} \text{ gs}^{-1}$.

At $\theta = -153^\circ$, the model is generally cooler than at apastron. The dayside temperature is around 15,180 K, while the night side temperature is around 15,030 K. The fact that the model cools down despite increasing XUV fluxes implies that a slow cooling process takes place after periastron that continues even after apastron. The circulation is qualitatively identical to the apastron model, but the maximum wind speed is slightly higher at 340 ms^{-1} . The thermal escape parameter increases to ~ 39 at the upper boundary, and the mass loss rate is $\sim 10^{-4} \text{ gs}^{-1}$.

Moving from $\theta = -153$ to periastron the model is heated by the steadily increasing XUV flux. Between these two positions, the flux is multiplied by a factor of 18. During periastron, the dayside temperature is 29,200-29,500 K, with a maximum on the equator, shifted slightly eastward from the substellar point. The night side temperature is around 26,800 K, implying that the diurnal temperature difference near transit should be of the order of 2,500 K. This implies that during periastron the XUV flux drives the model, instead of dynamics and slow cooling. The winds blow from the dayside to the night side, converging near the antistellar point, with a maximum speed of 2.8-3.2 kms⁻¹. The thermal escape parameter is 19, which indicates that the atmosphere is still in the thermal Jeans escape regime. The mass loss rate is $\sim 10^4$ gs⁻¹.

By the time the planet reaches $\theta = 153$ degrees, the thermosphere has started cooling down. At this point, the dayside temperature is around 23,430 K and the night side temperature is around 23,270 K. Thus the diurnal temperature difference is of the order of 150 K. As the upper thermosphere slowly cools, energy is advected around the planet and this mixing smoothes out the diurnal temperature difference that develops during periastron. Curiously, the day-night circulation is still symmetric about an axis connecting the substellar point to the antistellar point. The winds have slowed down to less than 200 ms⁻¹, and the thermal escape parameter has increased to ~ 23 at the upper boundary. The mass loss rate is $\sim 2 \times 10^3$ gs⁻¹.

3.3. Thermal Structure and Energy Balance

Figure 11 shows the substellar P-T profiles for the Exo-1 series at the four orbital positions discussed in the previous section. Outside periastron the P-T profiles are isothermal at pressures lower than about 0.2 nbar. Generally the temperature increases with altitude, and the gradient is steepest in the lower thermosphere at pressures higher than 0.3 μ bar. Overall, the temperatures are highest during periastron, and lowest during apastron. At $\theta = -153^\circ$ and at $\theta = 153^\circ$ the P-T profiles are identical in the upper thermosphere, but the lower thermosphere is warmer after periastron. During periastron the temperature rises sharply with altitude towards the upper boundary due to added XUV heating.

Figure 12 shows the substellar heating and cooling rates by volume for the Exo-1 simulations at the same orbital positions. Generally, in the middle and upper thermosphere (at $p < 0.1 \mu$ bar), the XUV heating is effectively balanced by H₃⁺ cooling. However, at pressures lower than 1.0 nbar, this cooling is less important due to non-LTE conditions, and the heating is balanced mainly by conduction of heat downward. In the lower thermosphere, the heating is balanced by the ‘triad’ of vertical advection, adiabatic expansion, and conduction. Due

to relatively low temperature, H_3^+ cooling is not that significant near the lower boundary. In the night side (not shown), the thermosphere is mainly heated by vertical downwelling and adiabatic contraction. The heating is balanced by vertical conduction.

In Figure 12, the solid line shows the net heating rate (the sum of all the energy equation terms) at each orbital position. The net heating rate is close to zero in the upper thermosphere, while variations take place in the lower thermosphere. The radiative timescale in the thermosphere is relatively short, and in those regions where H_3^+ cooling is significant, any added heating is quickly balanced by an adjustment in the cooling rate. This explains the rapid convergence of the Exo-1 simulations to steady state after only a few orbits. Circulation in the upper thermosphere is driven by uneven stellar irradiation, which explains the relatively steep diurnal temperature gradient.

In the lower thermosphere, on the other hand, net heating occurs during periastron. By the time the planet reaches $\theta = 153^\circ$ (0.22 AU), the lower thermosphere has started to cool down, due to conduction, advection and adiabatic expansion. The cooling continues until the model reaches $\theta = -153^\circ$. After this the model starts to heat up again as it moves towards periastron. The lower part of the model, instead of being radiation-driven, is dynamics-driven, and thus its response to the varying XUV fluxes is not as rapid as that of the upper thermosphere. Also, the diurnal temperature differences tend to disappear at high pressures, and as we have seen, the circumplanetary wind appears.

We define the radiative cooling function as the ratio of the total infrared cooling rate to the total XUV heating rate. This cooling function is relatively high for the Exo-1 simulations. During apastron, it is 78 %, and the total H_3^+ infrared emission rate (in all spectral lines) is 6.1×10^{14} W. At $\theta = -153^\circ$, the cooling function is 72% and the emission rate is 8.5×10^{14} W. During periastron, the corresponding figures are 85 % and 1.7×10^{16} W, respectively. Near the antitransit, and thus the possible secondary eclipse, the cooling function is 91 % and the emission rate is 1.1×10^{15} W. As a proxy for potentially detectable spectral lines, Shkolnik et al. (2006) estimated that the total H_3^+ emission rate should be of the order of 10^{17} - 10^{19} W if emissions are to be detected with current ground-based technology. This estimate is based on a sample of F, G, K, and M stars within a distance of ~ 40 pc. Unfortunately, even for these relatively high cooling functions, the predicted emission rates fall well short of the detection limits.

Figure 13 shows the substellar P-T profiles for the Exo-2 simulation at the same four orbital positions. Outside the periastron, the P-T profiles are isothermal at pressures lower than about 0.7 nbar, and during periastron the profile is isothermal at pressures lower than about 0.1 nbar. In the lower thermosphere, the temperature increases steadily with altitude. The temperature in the upper thermosphere increases as the planet moves towards periastron

from $\theta = -153^\circ$. The heating goes on for a while after periastron, but by the time the planet reaches $\theta = 153^\circ$, the outer layers have started to cool down. Curiously, this does not apply to the region between 3.0 and 100 nbar, where the model is actually warmer at $\theta = 153^\circ$ than it is during periastron. Towards apastron, the whole thermosphere cools down and this cooling continues until the planet reaches $\theta = -153^\circ$ again.

Figure 14 shows the corresponding volume heating and cooling rates for the above P-T profiles. The XUV heating (by volume) is concentrated near the bottom of the thermosphere. This is because, compared to H_2 , atomic hydrogen is not particularly effective in absorbing XUV radiation. Also, the heating efficiency in the outer envelope is only 10 %. The radiation thus penetrates to the H_2 -dominated bottom layers, where it is also absorbed by He, and where the heating efficiency is higher. However, the temperature is higher in the upper thermosphere, because the lower thermosphere is much denser and heats up sluggishly whereas even relatively inefficient heating is enough to produce high temperatures in the outer layers.

Generally, the stellar heating is balanced by vertical conduction, vertical advection and adiabatic expansion. In the night side, again, the heating is by downwelling and adiabatic contraction. H_3^+ cooling is negligible compared to other cooling mechanisms in the dayside, and generally it only occurs at the bottom of the thermosphere. As indicated by the net heating rates, the thermosphere heats up as it approaches periastron after $\theta = -153^\circ$, and the heating first occurs in the lower thermosphere. The model reaches temperature maximum after periastron, and by the time the planet reaches $\theta = 153^\circ$, the lower and upper thermospheres have started cooling down. Around the 100 nbar level XUV heating and vertical conduction are still heating the thermosphere at $\theta = 153^\circ$, and this is reflected in the P-T profiles above.

The radiative cooling functions are low for the whole orbit. At apastron, the cooling function is a meagre 0.23 % and the total H_3^+ emission rate is 4.9×10^{11} W. This is three orders of magnitude less than the emission rate for the Exo-1 apastron model. The cooling functions for $\theta = -153^\circ$, periastron, and $\theta = 153^\circ$ are 0.24, 0.097, and 0.19 %, respectively. The corresponding H_3^+ emission rates are 7.6×10^{11} W, 5.6×10^{12} W, and 6.3×10^{11} W.

3.4. Composition

Obviously, there are huge differences in thermospheric composition between the two scenarios, Exo-1 and Exo-2, with potentially observable consequences. Figure 15 shows the substellar number densities of the neutral species during apastron for both models. For

Exo-1, H_2 dominates at all levels. Atomic hydrogen overtakes helium around $0.1 \mu\text{bar}$ as the second most prominent neutral species. Qualitatively, this picture prevails throughout the whole orbit.

For Exo-2, atomic hydrogen is the dominant species at pressures lower than $1 \mu\text{bar}$, and at higher altitudes the concentrations of the other species are negligible. Intriguingly, helium dominates over H_2 at pressures between ~ 4 and 600 nbar . This is because the decline of H_2 in the upper thermosphere is not merely due to molecular diffusion, but it is significantly enhanced by thermal dissociation.

Figure 16 shows the substellar electron density profiles for Exo-1 and Exo-2, both during periastron and during apastron, and Figure 17 shows the corresponding ions density profiles for H^+ , H_2^+ , and H_3^+ . For Exo-1, the electron density during apastron increases with altitude in the lower thermosphere, and reaches a peak value of $\sim 1.8 \times 10^{13} \text{ m}^{-3}$ around 36 nbar . In general, the electron density is close to the density of H^+ , which is by far the dominant ion in the thermosphere. The electron density drops steeply in the night side in the lower thermosphere, but in the outer layers, the densities are fairly uniform around the whole atmosphere. This is because the lifetime of H^+ against recombination in the upper thermosphere is of the order of 40 hours, and the timescale for planetary rotation is similar. The relatively long lifetime of H^+ indicates that the assumption of photochemical equilibrium is inaccurate in the upper thermosphere, where ion transport is likely to be important. However, the lifetimes of other ions are relatively short, from seconds to minutes, and even the lifetime of H^+ is shorter in the lower thermosphere. The situation in this respect is thus similar to Jupiter, where H^+ densities also deviate from photochemical equilibrium in the upper thermosphere. The H_3^+ profile in Figure 17 has two distinct peaks, one between 0.7 and 5.0 nbar , and the other near the lower boundary. The substellar column densities of H^+ and H_3^+ are $7.9 \times 10^{18} \text{ m}^{-2}$ and $3.2 \times 10^{16} \text{ m}^{-2}$, respectively.

During periastron, there is a strong peak in the electron density profile near the $0.6 \mu\text{bar}$ level, with a density of $8.9 \times 10^{13} \text{ m}^{-3}$. This peak coincides with a H^+ peak in the lower thermosphere. Intriguingly, the electron and H^+ densities near the upper boundary are actually lower during periastron than they are during apastron. There are two main reasons for this. First, the temperature in the upper boundary region is higher during periastron, and this leads to a lower overall density. Second, the near-synchronisation of the planet’s spin leads to enhanced day-night circulation that increases the mixing ratio of H_2 in the dayside. The horizontal winds are fuelled by upwelling in the dayside and downwelling in the night side. Upwelling brings up gas from the lower thermosphere, where the mixing ratio of H_2 is higher, and thus replenishes H_2 concentrations at higher altitudes. Conversely, in the nightside the mixing ratio of atomic hydrogen is embellished as H_2 sinks

with downwelling. This kind of circulation is an important factor amplifying the cooling function in the thermospheres of tidally locked planets. During apastron, the mixing of the atmosphere is more effective, as the relative rotation of the planet with respect to the star is faster. This leads to more uniform mixing ratios of atomic hydrogen, which do not exhibit notable diurnal variations. For the periastron model, the substellar column densities of H^+ and H_3^+ are $2.0 \times 10^{19} \text{ m}^{-2}$ and $6.3 \times 10^{17} \text{ m}^{-2}$, respectively. The H_3^+ densities are quite a bit higher than at apastron, and the mixing ratio of ion is also higher in middle and upper thermosphere.

For Exo-2, during apastron, there are two peaks in the electron density profile at the bottom of the thermosphere and around 36 nbar, both with the roughly equal density of $6.3 \times 10^{13} \text{ m}^{-3}$. Overall, the electron densities are higher than in the Exo-1 simulation. As H^+ is virtually the only ion in the thermosphere, the electron density profile is effectively identical to the H^+ profile. The lifetime of H^+ in the upper thermosphere is around 90 hours, and a significant plasma density persists in the night side. This is such a large deviation from photochemical equilibrium that ion transport cannot be ignored. Unfortunately this means that our density plots are not likely to be accurate.

At pressures lower than about $0.6 \mu\text{bar}$, there is virtually no H_3^+ in the Exo-2 simulation. Very small amounts of H_2^+ are present, but the thermosphere does not contain enough H_2 to convert this into H_3^+ . In fact, the density of He^+ is generally higher in the thermosphere than the density of H_2^+ . The substellar column densities of H^+ and H_3^+ are $7.9 \times 10^{20} \text{ m}^{-2}$ and $5.0 \times 10^{14} \text{ m}^{-2}$, respectively.

During periastron, the peak electron densities are much higher, around $4.5 \times 10^{14} \text{ m}^{-3}$. The relative ion concentrations are similar to the apastron model. At pressures lower than $\sim 0.7 \text{ nbar}$, H^+ is actually the dominant species. In fact, the mixing ratio of H near the upper boundary, in relation to H^+ , is only 30 %. We have not made any provision for this in our simulations, which assume that the neutral density can be calculated from the ideal gas law, and that ionisation does not affect neutral mass fractions directly. This is a further reason to treat the Exo-2 ion densities with suspicion, at least during periastron. Elsewhere along the orbit, the density of H^+ tends to be much smaller compared to H.

One last uncertainty related to the calculations of neutral and ion densities in the Exo-2 series is the fact that the numerical solution for the neutral mass fractions uses H_2 as the ‘dominant’ species, although the equations themselves do *not* assume a dominant species and diffusion is calculated for three major species instead of minor species diffusion. However, the numerical solution evaluates the mass fractions for He and H, and then deduces those from unity in order to obtain the mass fraction for H_2 . This approach leads to numerical errors in the H-dominated part of the thermosphere. The problem is limited to the relatively

thin transition region between the H₂-dominated layers and the H-dominated layers. Above this region the mixing ratio of atomic hydrogen is unity for all practical purposes.

3.5. Variable temperatures

In order to explore the effect of variable lower boundary temperatures on our simulations, we generated a model, labelled Exo-3, which is otherwise identical to Exo-1 but where we varied the lower boundary temperature assuming that it is given by the equilibrium temperature of the planet (with a Bond albedo of 0.3) at different locations along the orbit. We updated this temperature at every time step during the simulation. Figure 18 shows the lower boundary temperature as a function of true anomaly and contrasts this with the globally averaged temperature at the upper boundary of the Exo-3 simulation. The equilibrium temperature varies from ~ 490 K at apastron to just over 1,100 K at periastron. This kind of variation, which is basically symmetric around the periastron, is unlikely to be realistic as the response of the lower atmosphere to varying stellar irradiation is likely to be more complex.

However, as Figure 18 indicates, varying the lower boundary temperature has almost no effect on the upper boundary temperatures. As it turns out, changing the lower boundary temperature does not affect the qualitative nature of the circulation and composition of the Exo-1 simulation either. Figure 18 also shows the substellar P-T profiles from the two simulations during periastron. At pressures between about $0.6 \mu\text{bar}$ and 1 nbar the P-T profiles coincide. Above the 1 nbar level, the Exo-3 model is slightly warmer, but the difference in temperature is barely noticeable. In the lower thermosphere the temperatures are obviously different due to the different lower boundary conditions. The XUV heating rates and the IR cooling rates in the two models are almost identical. In the lower thermosphere the dayside cooling effect due to vertical advection is slightly reduced in the Exo-3 model, while the cooling effect due to adiabatic expansion is enhanced. Also, due to the shallow vertical P-T profile near the lower boundary, the vertical conduction term produces slight heating near the lower boundary of the Exo-3 simulation. In conclusion, it seems that the effect of the higher lower boundary temperature in the Exo-3 simulation is dwarfed by the fact that the temperatures in the thermosphere are largely determined by radiative balance, and most of the XUV radiation is absorbed above the lower boundary.

We did not run a separate simulation to explore how the varying lower boundary temperature would affect the Exo-2 simulations, but as the upper boundary temperature in those simulations is consistently above 10,000 K, it is unlikely that a variation of a few 100 K at the lower boundary of the model would have a significant effect on the results.

4. Conclusions and Discussion

We have generated three-dimensional simulations of the upper atmosphere of HD17156b, by using an improved version of the coupled thermosphere-ionosphere model for extrasolar giant planets (EXOTIM) (Koskinen et al. 2007a,b). By adopting the model for this EGP that orbits its G-type host star on a highly eccentric orbit ($e = 0.67$), we have been able to make predictions about the nature and stability of its upper atmosphere, thermospheric dynamics and ion concentrations. These predictions have observable consequences and if followed up, they could prove very useful in probing the conditions in the atmosphere of this exotic world.

We have found that the composition of the thermosphere is sensitive to the composition of the underlying layers, and in particular to the mixing ratio of atomic hydrogen in the lower atmosphere. Due to molecular diffusion, we do not anticipate a significant presence of heavy molecules such as CO, CH₄ and N₂, that would lead to extensive and complicated photochemistry (eg. Garcia Munoz 2007), in the upper atmosphere. The availability of H₂ regulates the H₃⁺ cooling function in the thermosphere, and thus different mixing ratios of atomic hydrogen can lead to very different conditions in the upper atmosphere. Unfortunately, the mixing ratio of atomic hydrogen in the lower atmosphere is poorly constrained. Due to this uncertainty, we have generated two different types of HD17156b simulations: one with lower boundary mixing ratio of atomic hydrogen appropriate for Jupiter, and one with atomic hydrogen dominating the upper atmosphere.

In both cases, we find that the atmosphere of HD17156b remains stable everywhere along the orbit and does not begin to escape hydrodynamically. This is despite the fact that a planet with a circular orbit at the periastron distance of HD17156b (0.052 AU) from the host star would almost certainly develop a planetary wind similar to that observed on HD209458b. Evaporation is not as significant on HD17156b because the planet does not spend long enough within 0.1 AU from the parent star for hydrodynamic escape to begin. Also, it is three times as massive as Jupiter, and thus the escape velocity and the thermal energy required for escaping the atmosphere is relatively high.

Different thermospheric compositions, and thus different radiative cooling functions, lead very different conditions in the upper atmospheres. If the thermosphere is dominated mostly by H₂, the H₃⁺ cooling function varies between 70 and 90 % along the orbit, and the total infrared emissions are of the order of 10¹⁵-10¹⁶ W. In this case the extent of the atmosphere is negligible, and even the upper atmosphere stays relatively cool (2,000-3,000 K). The thermal escape parameter at the upper boundary ranges from 400 to 600, and this renders any kind of evaporation negligible. If, on the other hand, the thermosphere is dominated by H and H⁺, the radiative cooling function is only 0.1-0.24 %, and the total

infrared emissions are of the order of 10^{12} - 10^{13} W. In this case the upper atmosphere is hot (15,000-30,000 K) and during periastron, the atmosphere expands beyond $1.4 R_p$. Depending on the orbital position, the thermal escape parameter ranges from 14 to 40, indicating that the atmosphere is in the Jeans escape regime.

These predictions can *potentially* be verified by observations. The infrared emissions from H_3^+ are potentially observable in the future, and they would provide the most direct clue to the properties of the upper atmosphere and its interaction with the host star. Unfortunately, the predicted intensities are so low, that detection cannot be made with current ground-based technology (eg. Shkolnik et al. 2006). The extended atomic hydrogen cloud could possibly be observed by monitoring H Lyman α absorption during transit, which occurs near periastron. It is not clear, however, if such an observation is possible in the near future because the instrument that performed a similar measurement on HD209458b, i.e. STIS onboard HST, is no longer available.

Orbital dynamics and the planet’s spin affect three-dimensional simulations in many important ways. Circulation in the upper thermosphere is characterised by day-night winds, driven by a persistent diurnal temperature contrast. This behaviour is enhanced during periastron, when the planet is in near-synchronisation with the star. In the lower thermosphere, temperatures are fairly uniform horizontally and the circulation is characterised by an eastward, circumplanetary jet. In the H-dominated simulations, temperatures are generally more uniform and the wind speeds are slow.

As thermal escape is not as significant for HD17156b as it is for, say, HD2009458b, one wonders if non-thermal escape processes or tidal forces might come into play instead. Non-thermal escape arises from charge exchange with the impinging stellar wind, photodissociation or dissociative recombination, acceleration of ions along open magnetic field lines, sputtering of neutral particles or ion pick-up by the stellar wind, and impact ionisation and dissociation by stellar wind particles. Quantifying these effects for a planet like HD17156b is difficult, because there is no information about its magnetic field or the properties of the stellar wind in its vicinity. Estimates of non-thermal mass loss for a planet like HD209458b are of the order of 10^8 - 10^9 gs^{-1} (Erkaev et al. 2005). If similar values are to be expected for HD17156b, then evaporation from the planet is mostly non-thermal.

Adopting the formula presented by Erkaev et al. (2007), the approximate Roche lobe distance during periastron from HD17156b is 10-11 R_p . This means that the occurrence of so-called geometrical blow-off (Lecavelier des Etangs et al. 2004), driven by the tidal forces between the planet and the star, is very unlikely. In fact, it may be safe to ignore tidal forces in estimating the mass loss for HD17156b.

T. T. K. has been supported by UCL and Perren studentships, while A. D. A. and S. M. have been supported by the UK Science and Technology Facilities Council (STFC). This work was partly carried out on the Keter High Performance Computer System, which is managed by the Miracle Astrophysics Project and funded by STFC.

REFERENCES

- Achilleos, N., Miller, S., Tennyson, J., Aylward, A. D., Muller-Wodarg I. C. F., & Rees, D. 1998, *J. Geophys. Res.*, 103, 20089
- Anicich, V. G. 1993, *J. Phys. Chem. Ref. Data* 22, 1469
- Auerbach, D., Cacek, R., Candano, R., Gaily, T. D., Keyser, C. J., McGowan, J. W., Mul, P. M., & Wilk, S. F. J. 1977, *J. Phys. B At. Mol. Phys.*, 10, 3797
- Ballester, G. E., Sing, D. K., & Herbert, F. 2007, *Nature*, 445, 511
- Banks, P. M., & Kockarts, G. 1973, *Aeronomy* (New York, USA: Academic Press)
- Barbieri, M., et al. 2007, *A&A*, 476, L13
- Baulch, D. L., et al. 1992, *J. Phys. Chem. Ref. Data* 21, 411
- Cecchi-Pestellini, C., Ciaravella, A., & Micela, G. 2006, *A&A*, 458, L13
- Chung, Y. M., Lee, E.-M., Masuoka, T., & Samson, J. A. R. 1993, *J. Chem. Phys.*, 99, 885
- Datz, S., Sundstrom, G., Biedermann, C., Brostrom, L., Danared, H., Mannervik, S., Mowat, J. R., & Larsson, M. 1995, *Phys. Rev. Lett.*, 74, 896
- Dinelli, B. M., Miller, S., & Tennyson, J. 1992, *J.Mol.Spectros.*, 153, 718
- Dujardin, G., Besnard, L., Hellner, L., & Malinovitch, Y. 1987, *Phys. Rev. A*, 35, 5012
- Erkaev, N. V., Penz, T., Lammer, H., Lichtenegger, H. I. M., Biernat, H. K., Wurz, P., Griesmeir, J.-M., & Weiss, W. W. 2005, *ApJS*, 157, 396
- Erkaev, N. V., Kulikov, Y. N., Lammer, H., Selsis, F., Langmayr, D., Jaritz, G. F., & Biernat, H. K. 2007, *A&A*, 472, 329
- Fischer, D. A., et al. 2005, *ApJ*, 620, 481
- Fischer, D. A., et al. 2007, *ApJ*, 669, 1336

- Garcia Munoz, A. 2007, *Planet. Space Sci.*, 55, 1426
- Gillon, M., Triaud, A. H. M. J., Mayor, M., Queloz, D., Udry, S., & North, P. 2007, preprint (arXiv:0712.2073)
- Grodent, D., Hunter Waite, J., Jr., & Gerard, J. C. 2001, *J. Geophys. Res.*, 106, 12933
- Ham, D. O., Trainor, D. W., & Kaufman, F. 1970, *J. Chem. Phys.*, 53, 4395
- Hummer, D. G., & Seaton, M. J. 1963, *MNRAS*, 125, 437
- Hunten, D. M. 1973, *J. Atmos. Sci.*, 30, 1481
- Hut, P. 1981, *A&A*, 30, 1481
- Irwin, J., et al. 2008, preprint (arXiv:0801.1496)
- Kapras, Z., Anicich, V. G., & Huntress, W. T. 1979, *J. Chem. Phys.*, 70, 2877
- Kim, Y. H., & Fox, J. L. 1994, *Icarus*, 112, 310
- Koskinen, T. T., Aylward, A. D. A., Smith, C. G. A., Miller, S. 2007a, *ApJ*, 661, 515
- Koskinen, T. T., Aylward, A. D. A., Miller, S. 2007b, *Nature*, 450, 845
- Langton, J., & Laughlin, G. 2008, *A&A*, 483, L2
- Lecavelier des Etangs, A., Vidal-Madjar, A., McConnell, J. C., & Hebrard, G. 2004, *A&A*, 418, L1
- Liang, M.-C., Parkinson, C. D., Lee, A. Y.-T., Yung, Y. L., & Seager, S. 2003, *ApJ*, 596, 247
- Moses, J. I., & Bass, S. F. 2000, *J. Geophys. Res.*, 105, 7013
- Neale, L., Miller, S., & Tennyson, J. 1996, *ApJ*, 464, 516
- Penz, T., Micela, G., & Lammer, H. 2008, *A&A*, 477, 309
- Press, W. H., Teukolsky, S. A., Vetterling, W. T., & Flannery, B. P. 1992, *Numerical Recipes in Fortran: The Art of Scientific Computing* (2nd ed.; Cambridge, UK: Cambridge University Press)
- Ribas, I., Guinan, E. F., Gudel, M., & Audard, M. 2005, *ApJ*, 622, 680

- Schneider, E. M., Velazquez, P. F., Esquivel, A., Raga, A. C., & Blanco-Cano, X. 2007, *ApJ*, 671, 57
- Seagroves, S., Harker, J., Laughlin, G., Lacy, J., & Castellano, T. 2003, *PASP*, 115, 1355
- Shapiro, R. 1970, *Rev. Geophys. and Space Phys.*, 8, 359
- Shkolnik, E., Gaidos, E., & Moskovitz, N. 2006, *AJ*, 132, 1267
- Storey, P. J., & Hummer, D. G. 1995, *MNRAS*, 272, 41
- Sundstrom, G., et al. 1994, *MNRAS*, 263, 785
- Thread, L. P., & Huntress, W. P. 1974, *J. Chem. Phys.*, 60, 2840
- Tian, F., Toon, O. B., Pavlov, A. A., & De Sterck, H. 2005, *ApJ*, 621, 1049
- Tobiska, W. K., Woods, T., Eparvier, F., Viereck, R., Floyd, L., Bouwer, D., Rottman, G., & White, O. R. 2000, *J. Atmos. Solar Terr. Phys.*, 62, 1233
- Vidal-Madjar, A., Lecavrier des Etangs, A., Desert, J.-M., Ballester, G. E., Ferlet, R., Hebrard, G., & Mayor, M. 2003, *Nature*, 422, 143
- Vidal-Madjar, A., et al. 2003, *ApJ*, 604, L69
- Vidal-Madjar, A., Lecavelier des Etangs, A., Desert, J.-M., Ballester, G. E., Ferlet, R., Hebrard, G., & Mayor, M. 2008, *ApJ*, 676, L57
- Waite, J. H., Jr., Cravens, T. E., Kozyra, J., Nagy, A. F., Atreya, S. K., & Chen, R. H. 1983, *J. Geophys. Res.*, 88, 6143
- Yan, M., Sadeghpour, H. R., & Dalgarno, A. 1998, *ApJ*, 496, 1044
- Yelle, R. V. 2004, *Icarus*, 170, 167
- Yelle, R. V. 2006, *Corrigendum, Icarus*, 183, 508

Table 1. Chemical reactions used by the model.

Reaction	Rate ^{a,b}	Reference
1. $\text{H}_2 + h\nu \rightarrow \text{H}_2^+ + \text{e}$	-	Yan et al. (1998)
2. $\text{H}_2 + h\nu \rightarrow \text{H}^+ + \text{H} + \text{e}$	-	Chung et al. (1993), Dujardin et al. (1987)
3. $\text{H}_2 + h\nu \rightarrow \text{H}^+ + \text{H}^+ + \text{e}$	-	Dujardin et al. (1987)
4. $\text{H} + h\nu \rightarrow \text{H}^+ + \text{e}$	-	Hummer et al. (1963)
5. $\text{He} + h\nu \rightarrow \text{He}^+ + \text{e}$	-	Yan et al. (1998)
6. $\text{H}_2 + \text{M} \rightarrow 2\text{H} + \text{M}$	$1.5 \times 10^{-9} \exp(-4.8e4/T)$	Baulch et al. (1992)
7. $2\text{H} + \text{M} \rightarrow \text{H}_2 + \text{M}$	$8.0 \times 10^{-33} (300/T)^{0.6}$	Ham et al. (1970)
8. $\text{H}^+ + \text{H}_2 (\nu \geq 4) \rightarrow \text{H}_2^+ + \text{H}$	$1.0 \times 10^{-9} \exp(-2.19e4/T)$	Yelle (2004), estimated
9. $\text{H}_2^+ + \text{H}_2 \rightarrow \text{H}_3^+ + \text{H}$	2.0×10^{-9}	Thread & Huntress (1974)
10. $\text{H}^+ + \text{H}_2 + \text{M} \rightarrow \text{H}_3^+ + \text{M}$	3.2×10^{-29}	Kim & Fox (1994)
11. $\text{He}^+ + \text{H}_2 \rightarrow \text{H}^+ + \text{H} + \text{He}$	$1.0 \times 10^{-9} \exp(-5700/T)$	Moses & Bass (2000)
12. $\text{He}^+ + \text{H}_2 \rightarrow \text{H}_2^+ + \text{He}$	9.35×10^{-15}	Anicich (1993)
13. $\text{H}_3^+ + \text{H} \rightarrow \text{H}_2^+ + \text{H}_2$	2.0×10^{-9}	Yelle (2004), estimated
14. $\text{H}_2^+ + \text{H} \rightarrow \text{H}^+ + \text{H}_2$	6.4×10^{-10}	Kapras et al. (1979)
15. $\text{H}^+ + \text{e} \rightarrow \text{H} + h\nu$	$4.0 \times 10^{-12} (300/T_e)^{0.64}$	Storey & Hummer (1995)
16. $\text{H}_2^+ + \text{e} \rightarrow \text{H} + \text{H}$	$2.3 \times 10^{-8} (300/T_e)^{0.4}$	Auerbach et al. (1977)
17. $\text{He}^+ + \text{e} \rightarrow \text{He} + h\nu$	$4.6 \times 10^{-12} (300/T_e)^{0.64}$	Storey & Hummer (1995)
18. $\text{H}_3^+ + \text{e} \rightarrow \text{H}_2 + \text{H}$	$2.9 \times 10^{-8} (300/T_e)^{0.64}$	Sundstrom et al. (1994)
19. $\text{H}_3^+ + \text{e} \rightarrow \text{H} + \text{H} + \text{H}$	$8.6 \times 10^{-8} (300/T_e)^{0.64}$	Datz et al. (1995)

^aPhoto-ionisation rates are calculated explicitly by using the photoionisation cross sections given in the references.

^bTwo-body rates are given in cm^3s^{-1} and three-body rates are given in cm^6s^{-1} . The electron temperatures are assumed to be the same as neutral temperatures.

Table 2. Non-LTE correction factors

Pressure (nbar)	Temperature (K)	Detailed balance	Experimental
2000	520	1.00	1.00
1340	833	1.00	1.00
899	1112	1.00	1.00
602	1382	0.998	1.00
404	1614	0.986	1.00
271	1732	0.971	1.00
181	1792	0.956	1.00
121	1849	0.934	1.00
82	1925	0.907	1.00
55	2008	0.870	0.878
36	2083	0.824	0.782
25	2147	0.767	0.696
16	2201	0.702	0.618
11	2252	0.630	0.548
7.4	2311	0.556	0.484
5.0	2382	0.480	0.426
3.3	2465	0.404	0.374
2.2	2555	0.330	0.327
1.5	2654	0.258	0.284
1.0	2766	0.194	0.245
0.67	2899	0.138	0.210
0.45	3074	0.0916	0.179
0.30	3314	0.0554	0.150
0.20	3615	0.0303	0.124
0.14	3919	0.0155	0.101
0.09	4144	0.0082	0.0794
0.06	4254	0.0050	0.0602
0.04	4254	0.0036	0.0428

Table 3. Planetary and orbital parameters for HD17156b

Planetary parameters^a	
M_p (M_{Jup})	3.1
R_p (R_{Jup})	0.96
Orbital parameters^a	
Eccentricity	0.67
Semi-major axis (AU)	0.16
Inclination ($^\circ$)	85.4
Period (days)	21.2
Longitude of periastron ($^\circ$)	121
Lower boundary conditions	
T_0 (K)	520.0
p_0 (Pa)	0.2
Gravity (ms^{-2})	87.0
Mixing ratio of H (Exo-1)	2×10^{-4}
Mixing ratio of H (Exo-2)	0.01

^aWith the exception of the planetary radius, the orbital and planetary parameters were taken from Gillon et al. (2007). Note that Gillon et al. (2007) have recently published and estimated radius of $1.23^{+0.17}_{-0.2} R_{Jup}$ for the planet. The value given by Irwin et al. (2008) is $1.01 \pm 0.09 R_{Jup}$. Thus, given the error ranges, these two estimates coincide. We have used a value that agrees with the estimates given by Irwin et al. (2008).

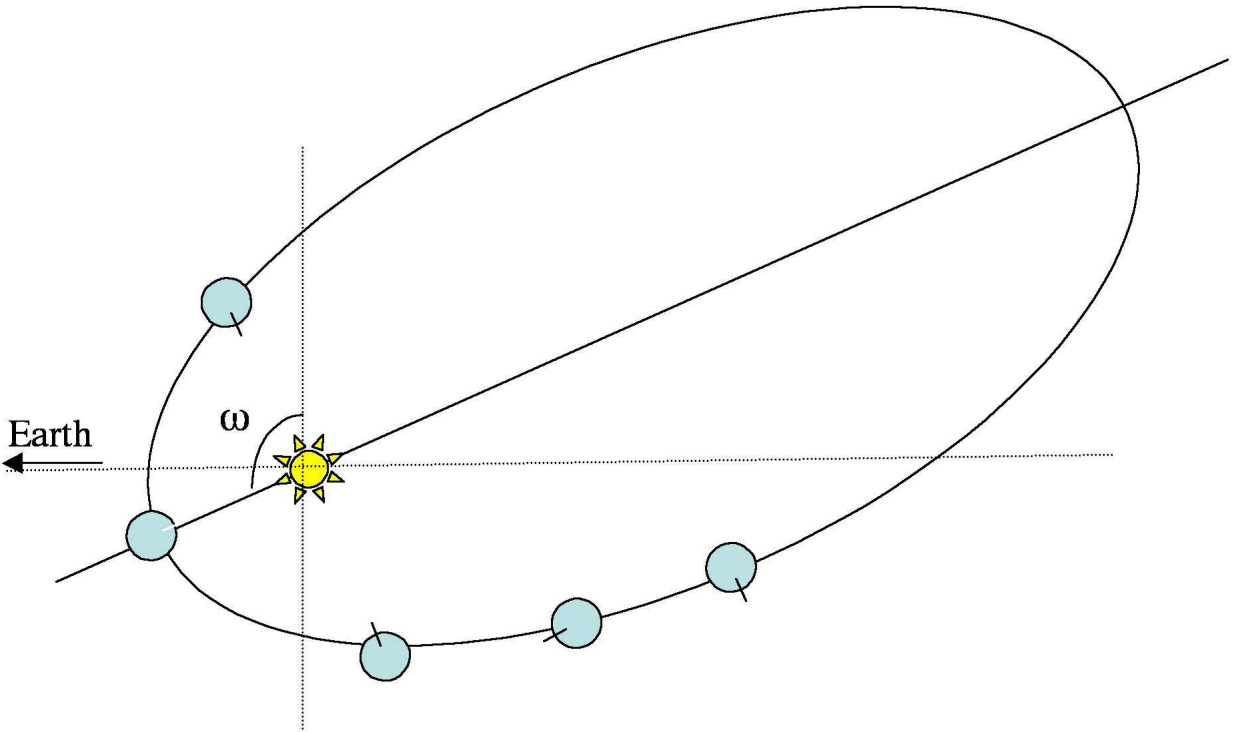


Fig. 1.— The orbit of HD17156b. Note that the orbit is not drawn to scale and is meant for illustration purposes only. The planet is shown at different positions near periastron to illustrate ‘pseudo-synchronous’ rotation. During the periastron the same side of the planet always faces the star, but as the planet moves farther from true anomaly of 90° , it begins to rotate asynchronously. The angle ω marks the longitude of the periastron.

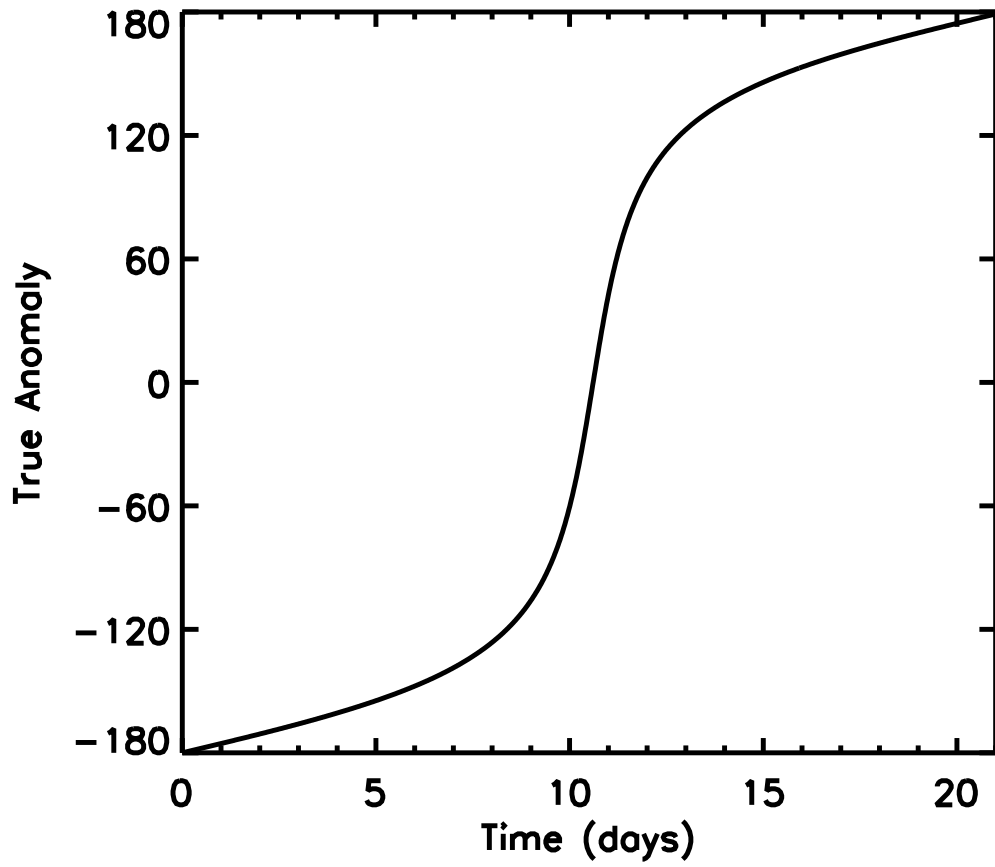


Fig. 2.— Orbital true anomaly versus time (in Earth days). The orbital period of HD17156b is approximately 21.2 Earth days. Periastron is located at $\theta = 0$. The planet spends only ~ 2 days within 0.1 AU, passing through periastron.

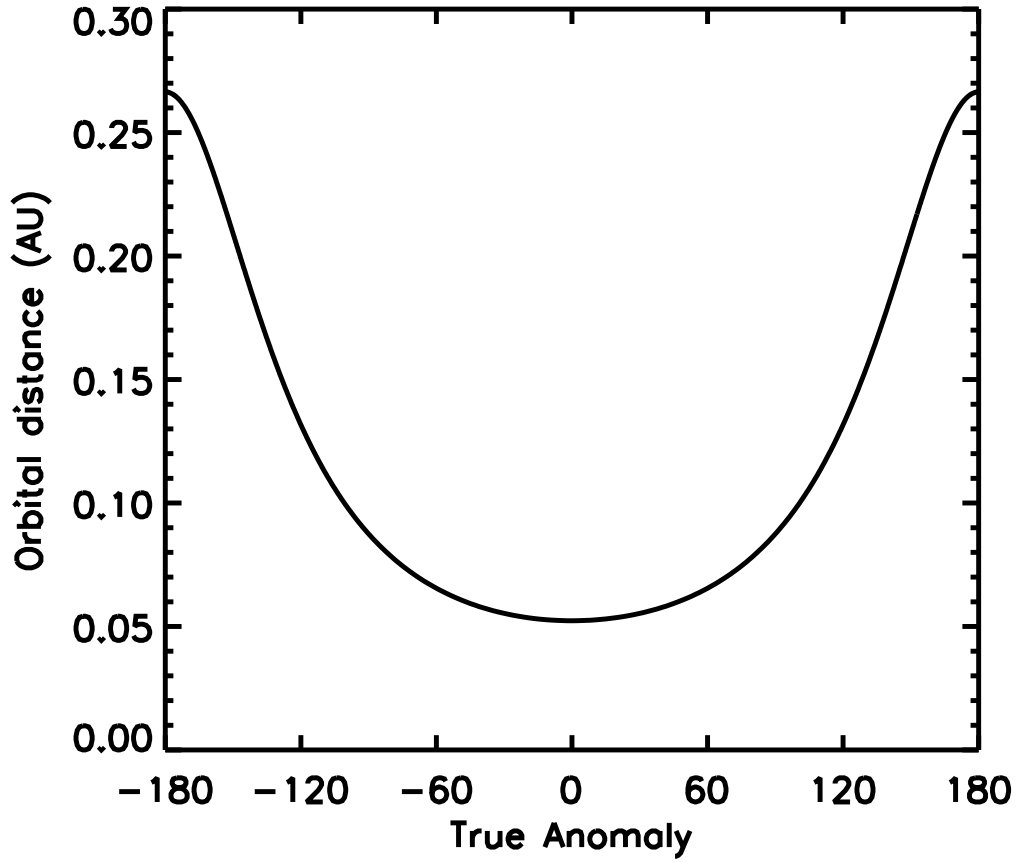


Fig. 3.— Orbital distance (in AU) versus true anomaly. The orbital period of HD17156b is approximately 21.2 Earth days. Periastron is located at $\theta = 0$.

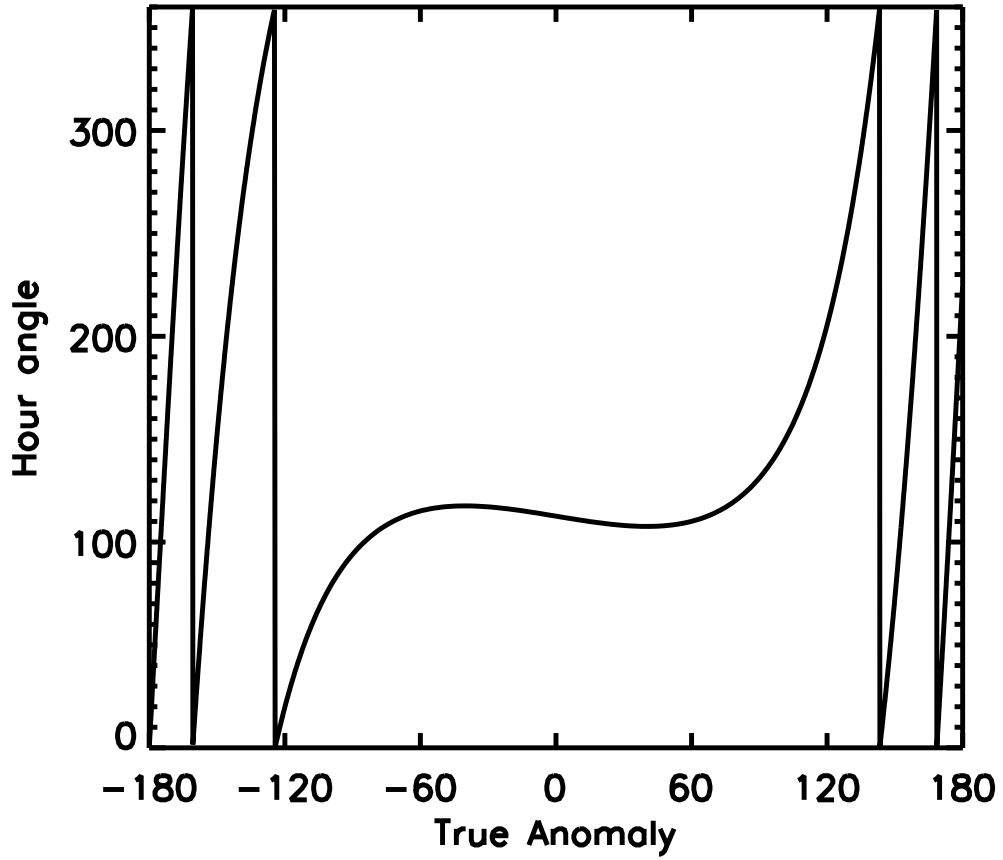


Fig. 4.— Hour angle versus orbital true anomaly. Here the hour angle traces the angular separation of a fixed point on the planet’s surface and the substellar point. Zero and 360 degrees correspond to the substellar point.

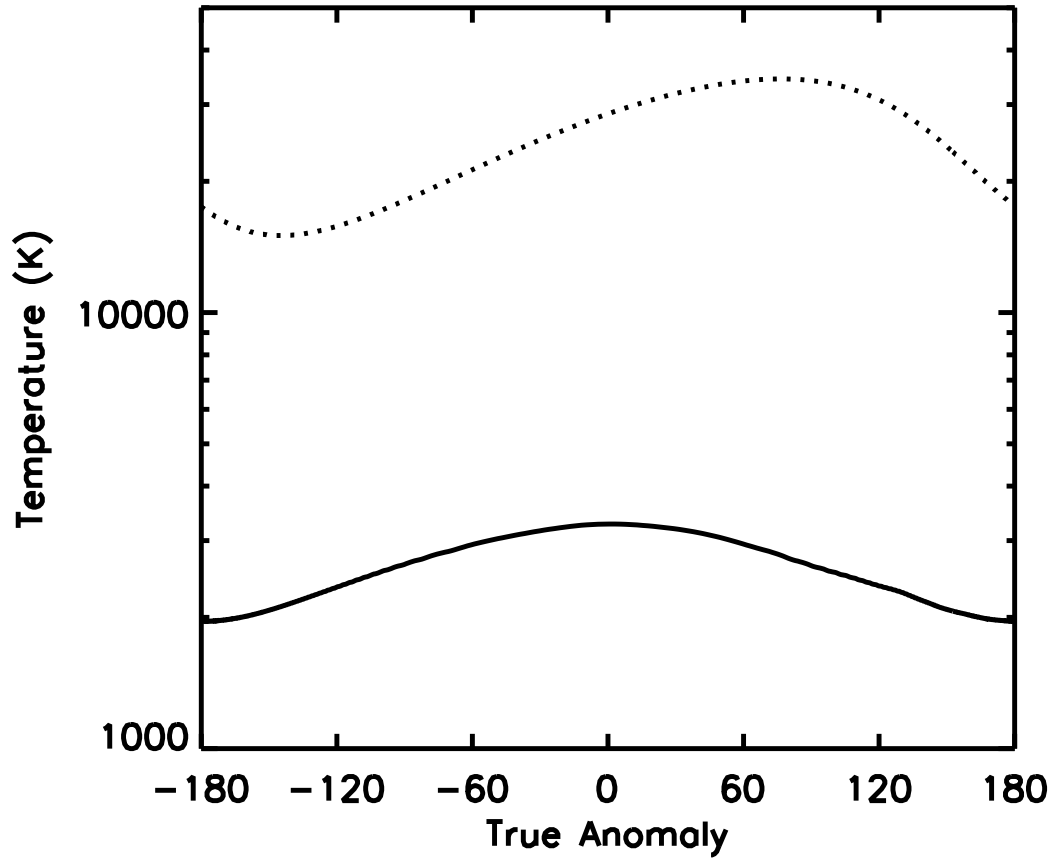


Fig. 5.— Globally averaged upper boundary (at 0.04 nbar) temperatures for two different simulations with different lower boundary mixing ratios of atomic hydrogen and radiative cooling functions. The solid line shows temperatures for a model with a cooling function of 70-90 % and the dotted line shows temperatures for a model with a cooling function of 0.01-0.24 % (see text).

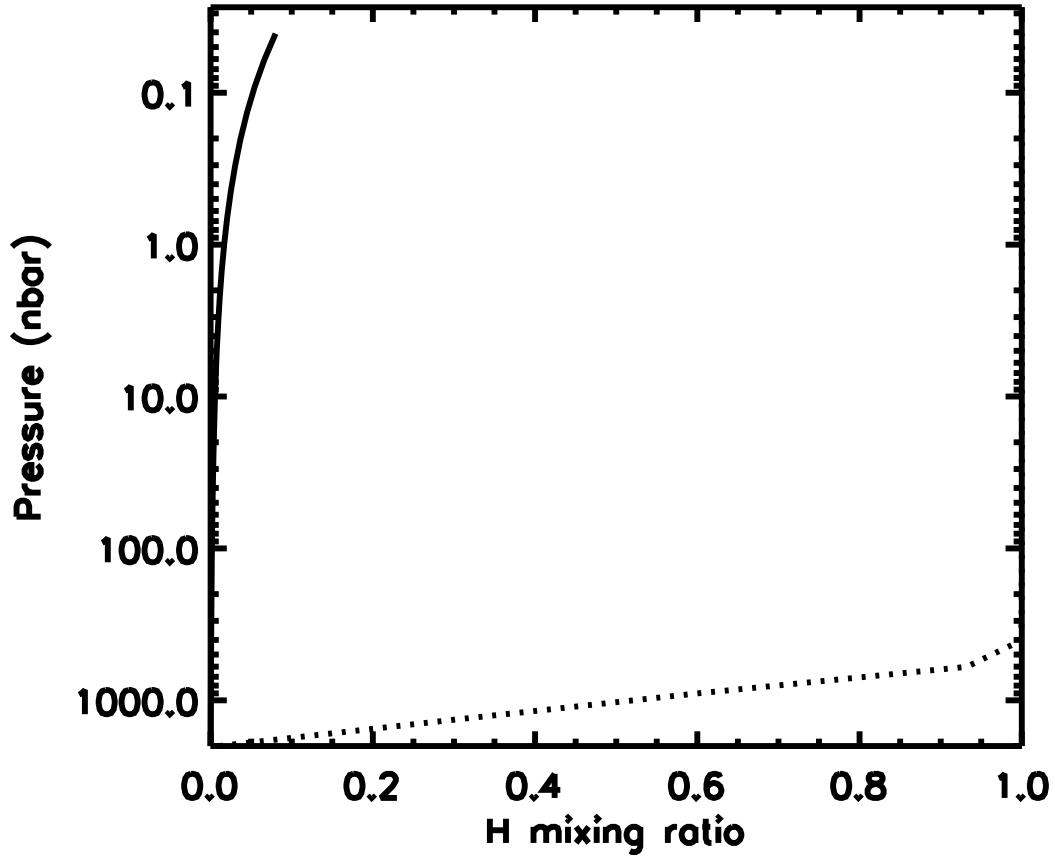


Fig. 6.— The mixing ratio of atomic hydrogen at the substellar point of Exo-1 (solid line) and Exo-2 (dotted line) during apastron.

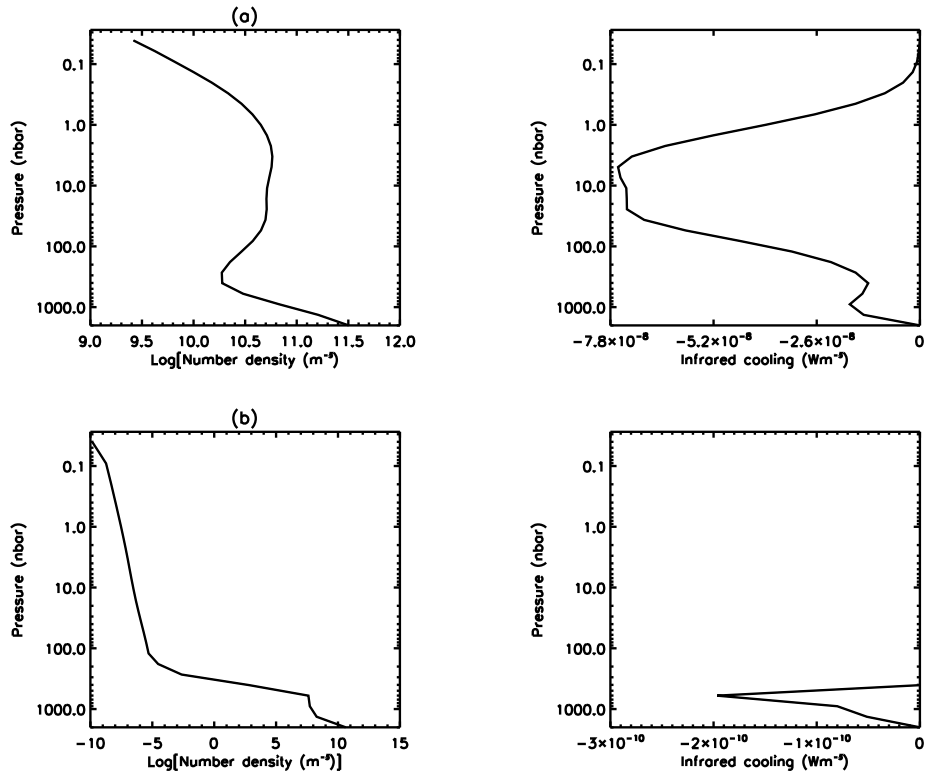
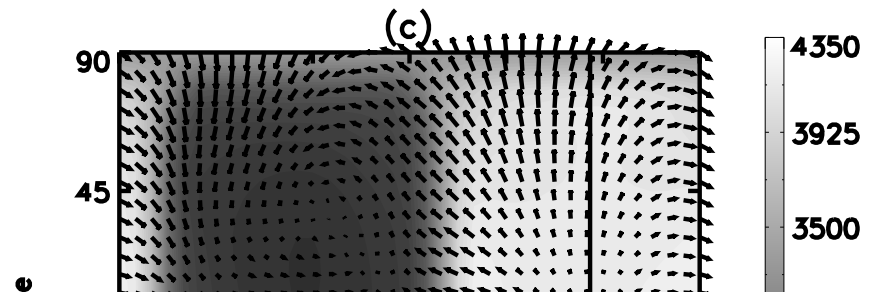
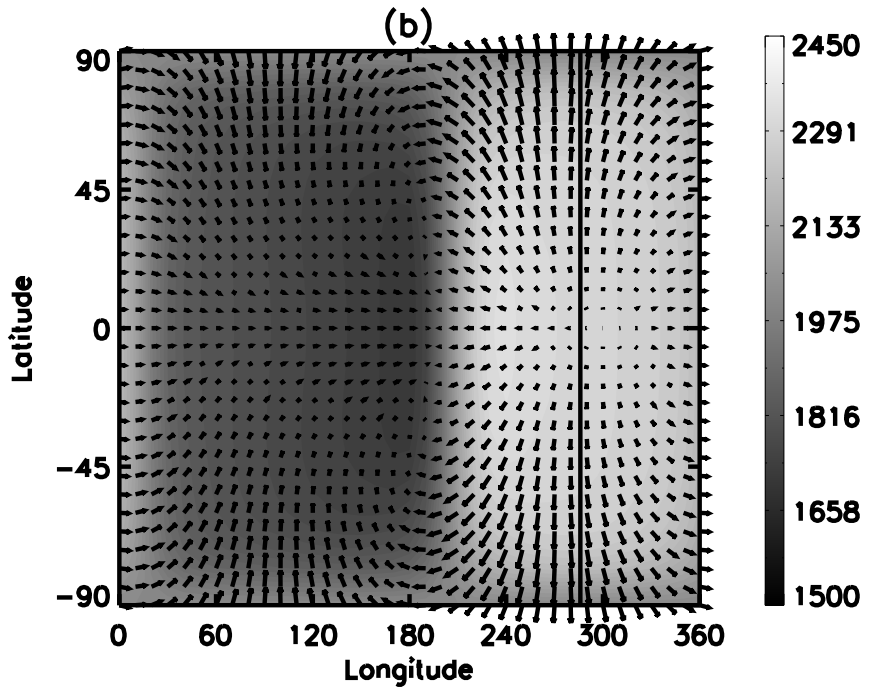
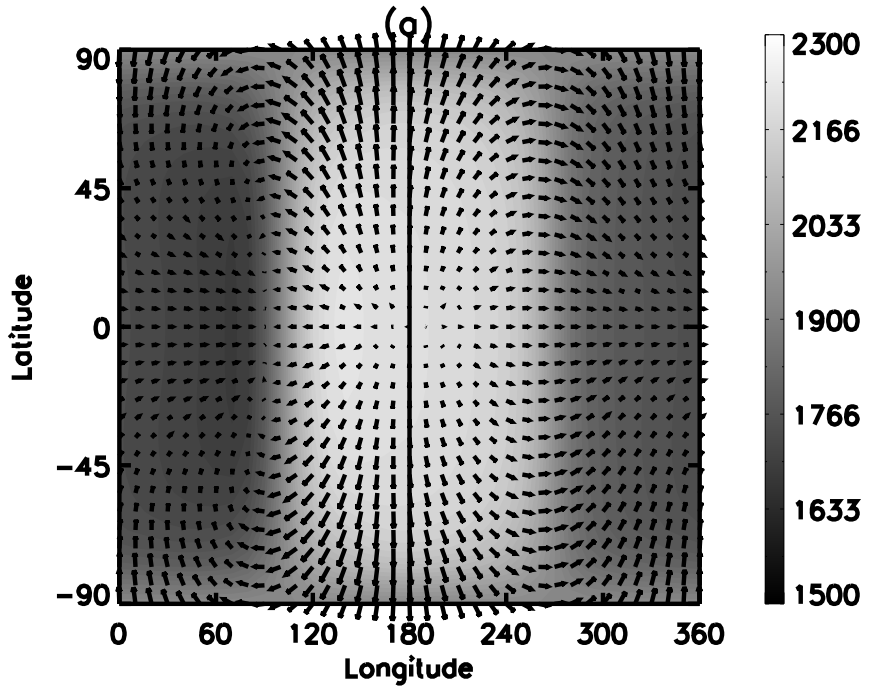
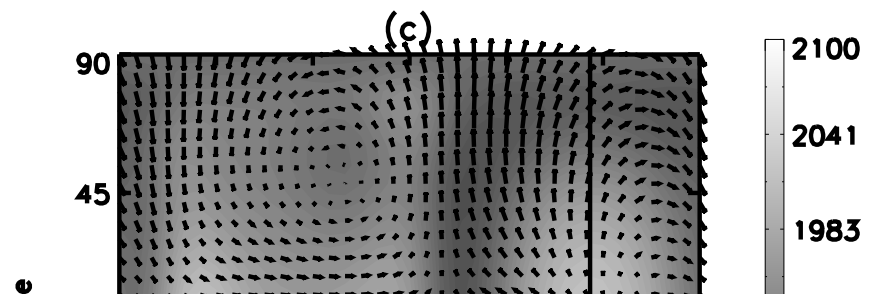
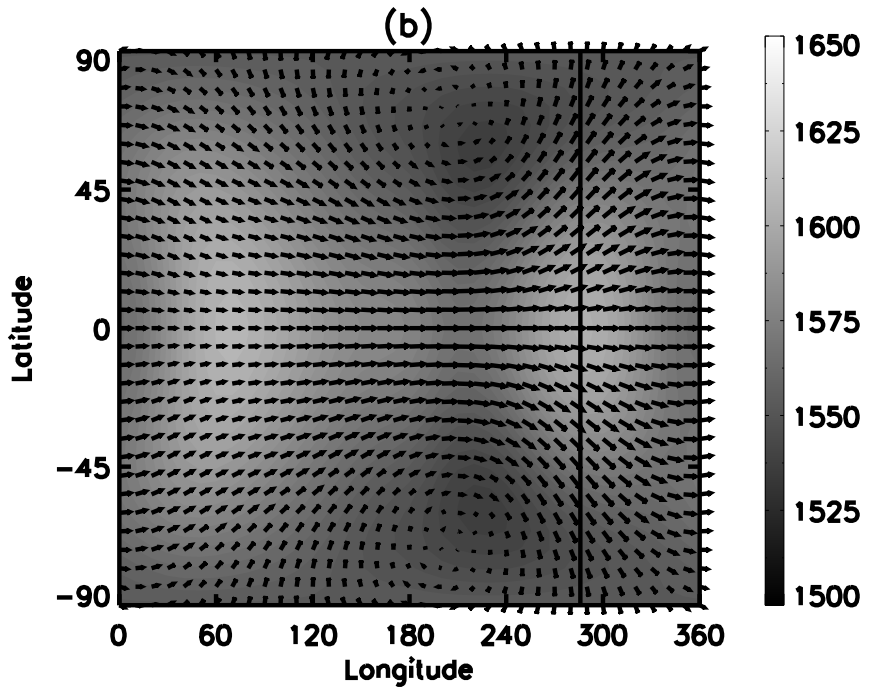
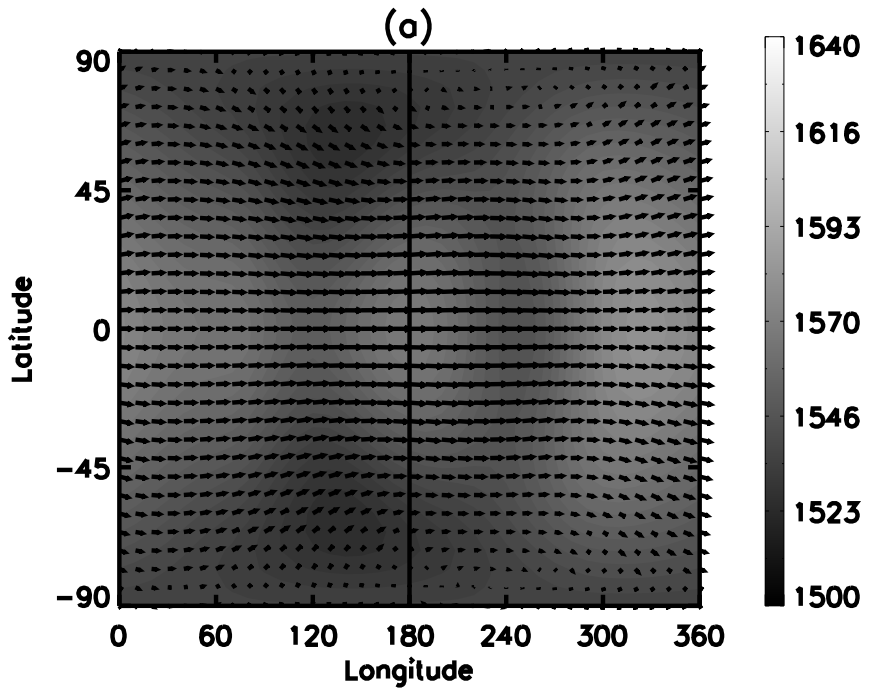
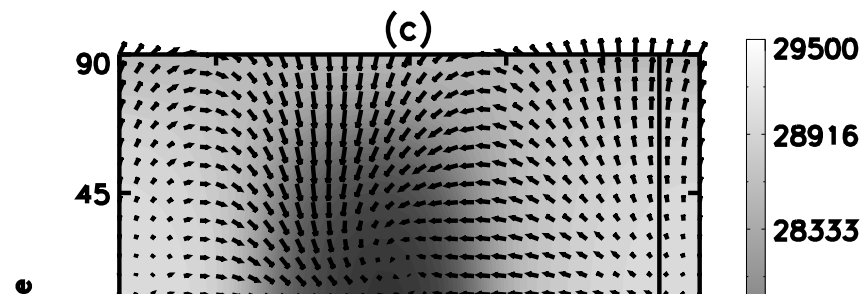
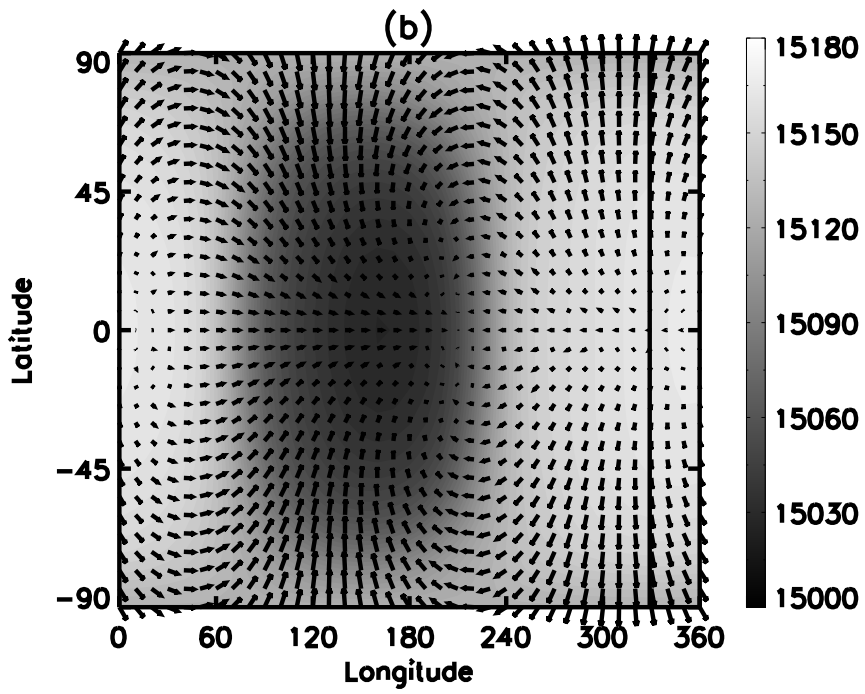
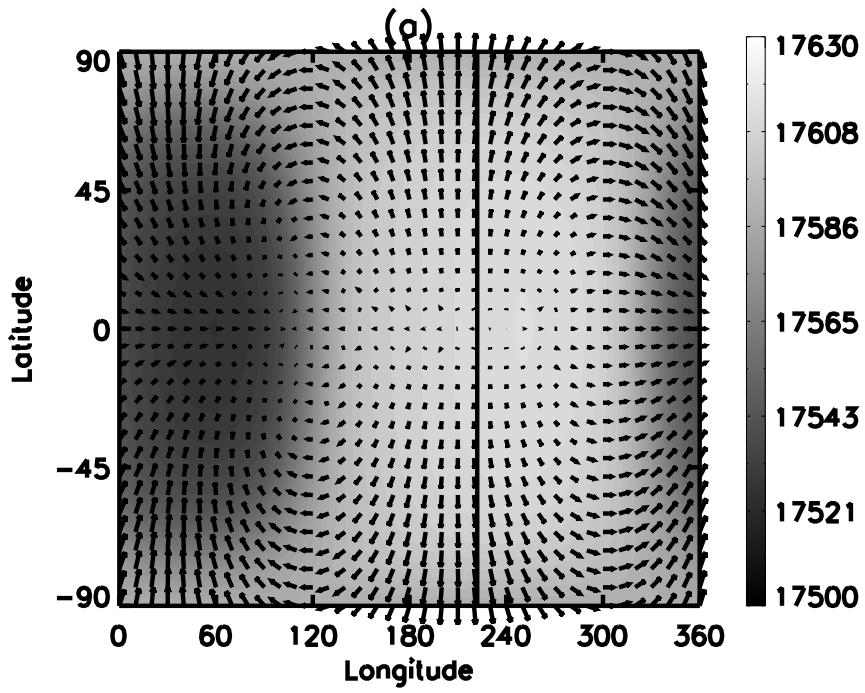


Fig. 7.— H_3^+ densities and the corresponding volume infrared cooling rates for (a) Exo-1 and (b) Exo-2 (see text) during apastron at the substellar point.







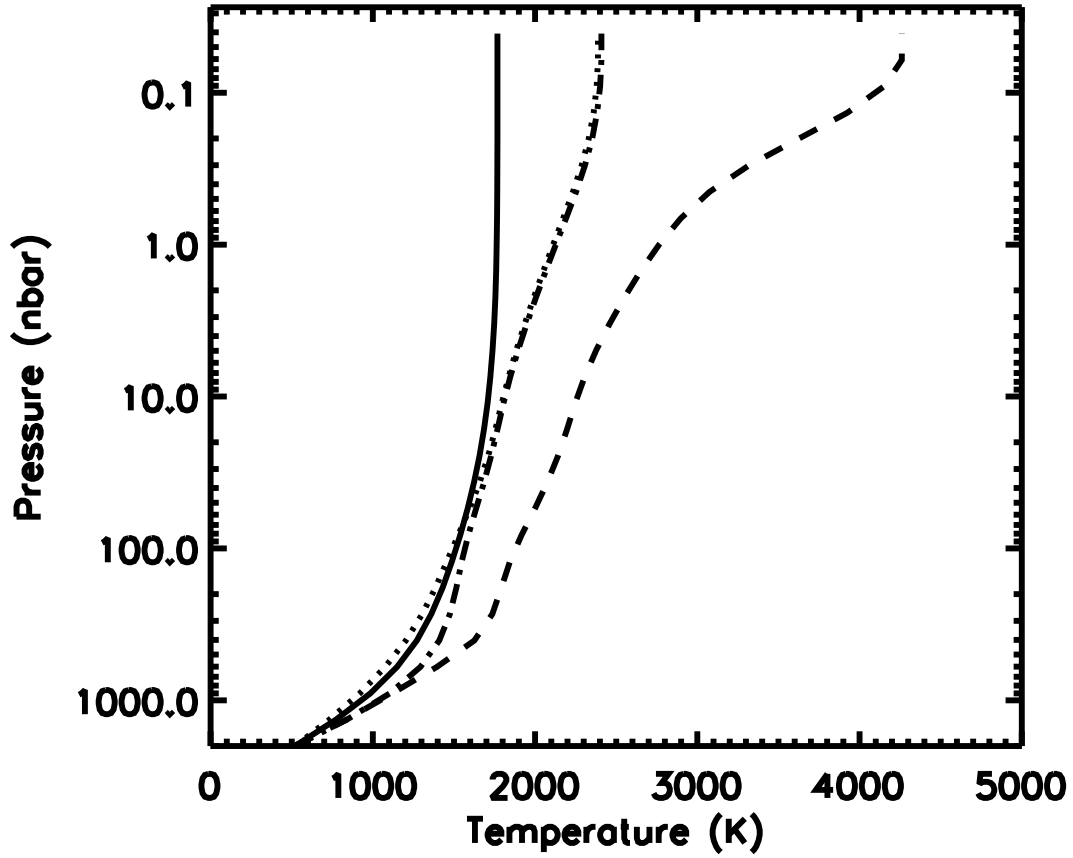


Fig. 11.— Substellar P-T profiles for the Exo-1 simulations at apastron (solid line), $\theta = -153^\circ$ (dotted line), periastron (dashed line), and $\theta = 153^\circ$ (dash-dotted line).

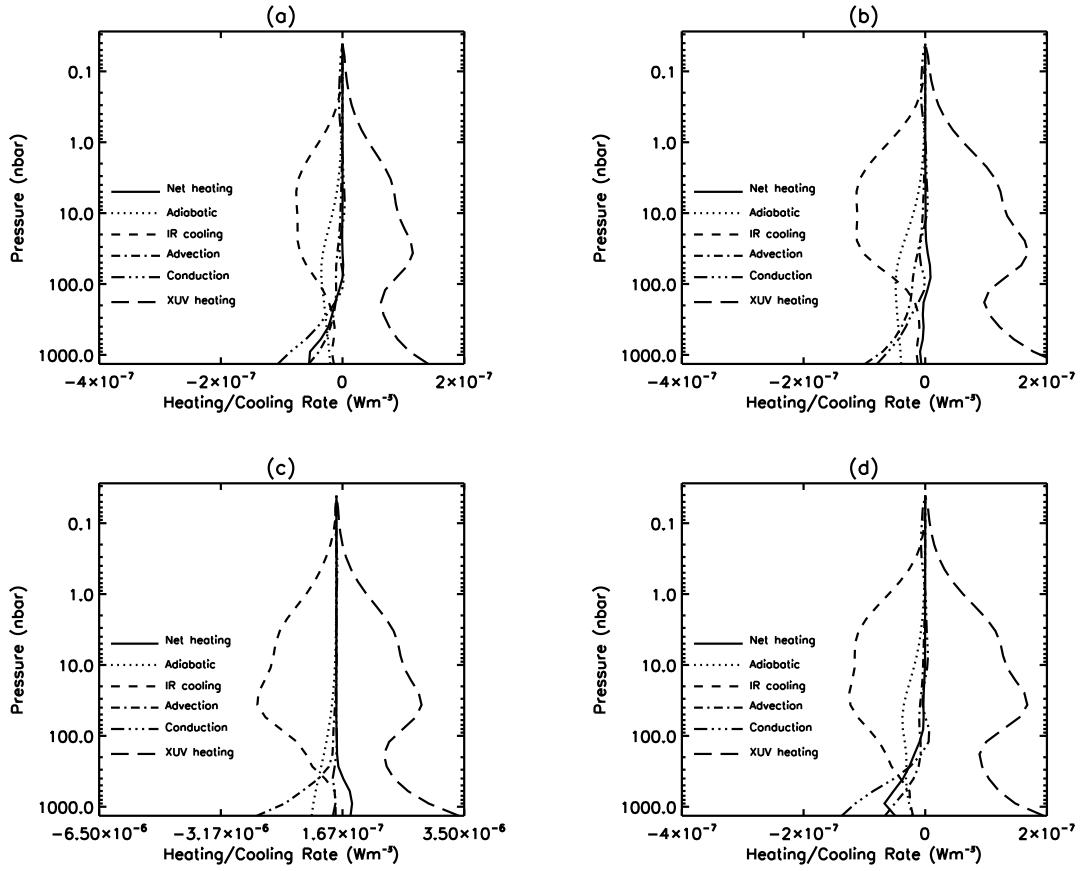


Fig. 12.— Substellar energy equation terms (per unit volume) for the Exo-1 simulations at (a) apastron, (b) $\theta = -153^\circ$, (c) periastron, and (d) $\theta = 153^\circ$.

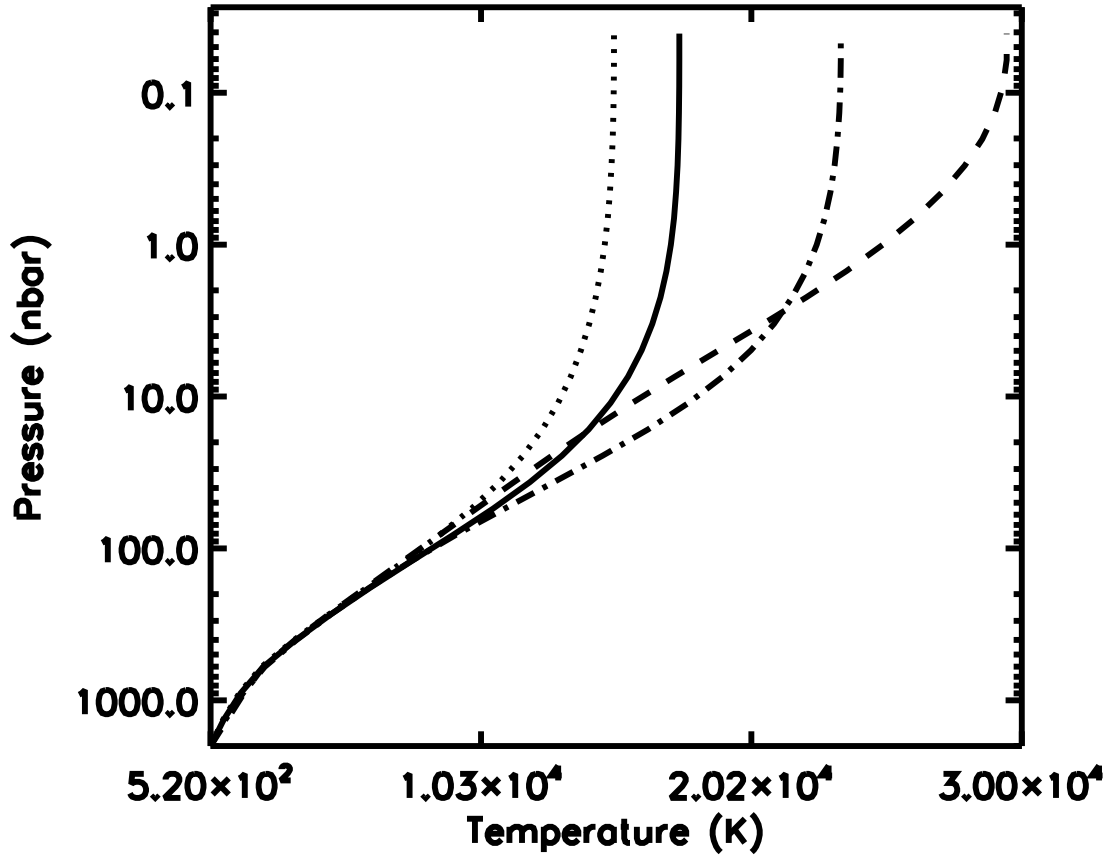


Fig. 13.— Substellar P-T profiles for the Exo-2 simulations at apastron (solid line), $\theta = -153^\circ$ (dotted line), periastron (dashed line), and $\theta = 153^\circ$ (dash-dotted line).

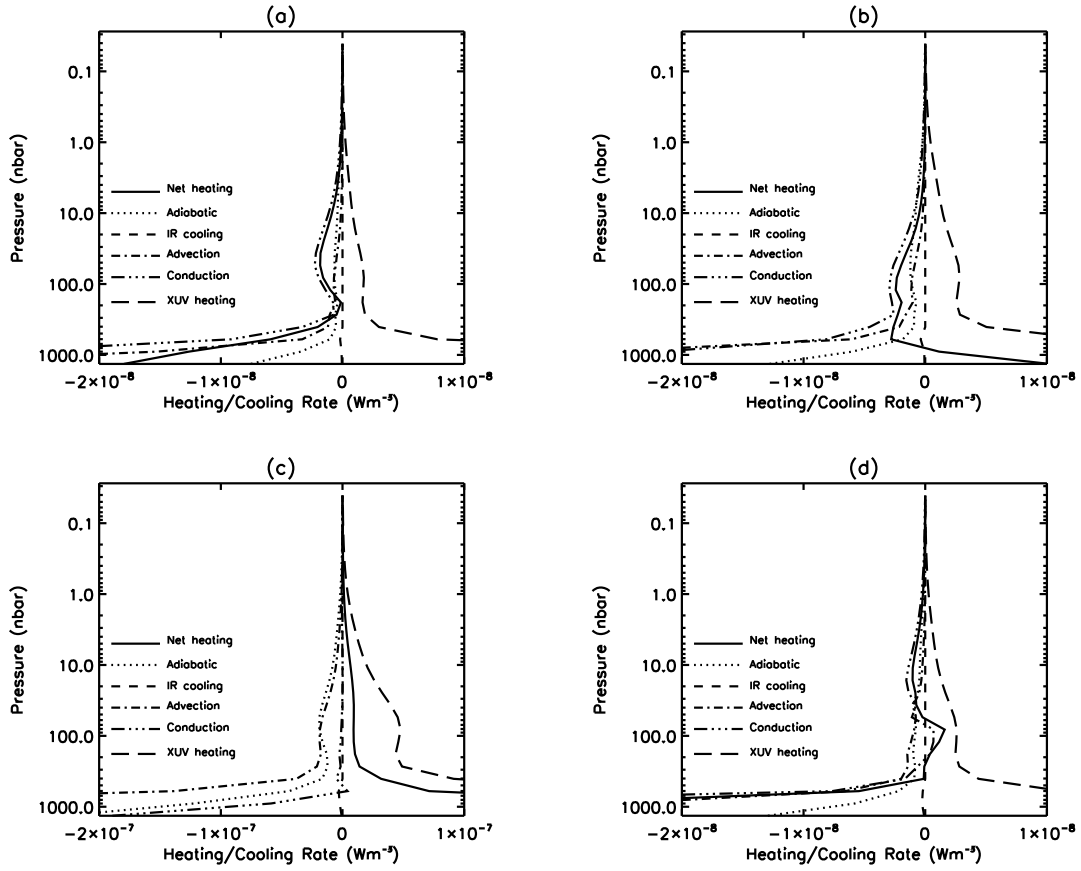


Fig. 14.— Substellar energy equation terms (per unit volume) for the Exo-2 simulations at (a) apastron, (b) $\theta = -153^\circ$, (c) periastron, and (d) $\theta = 153^\circ$.

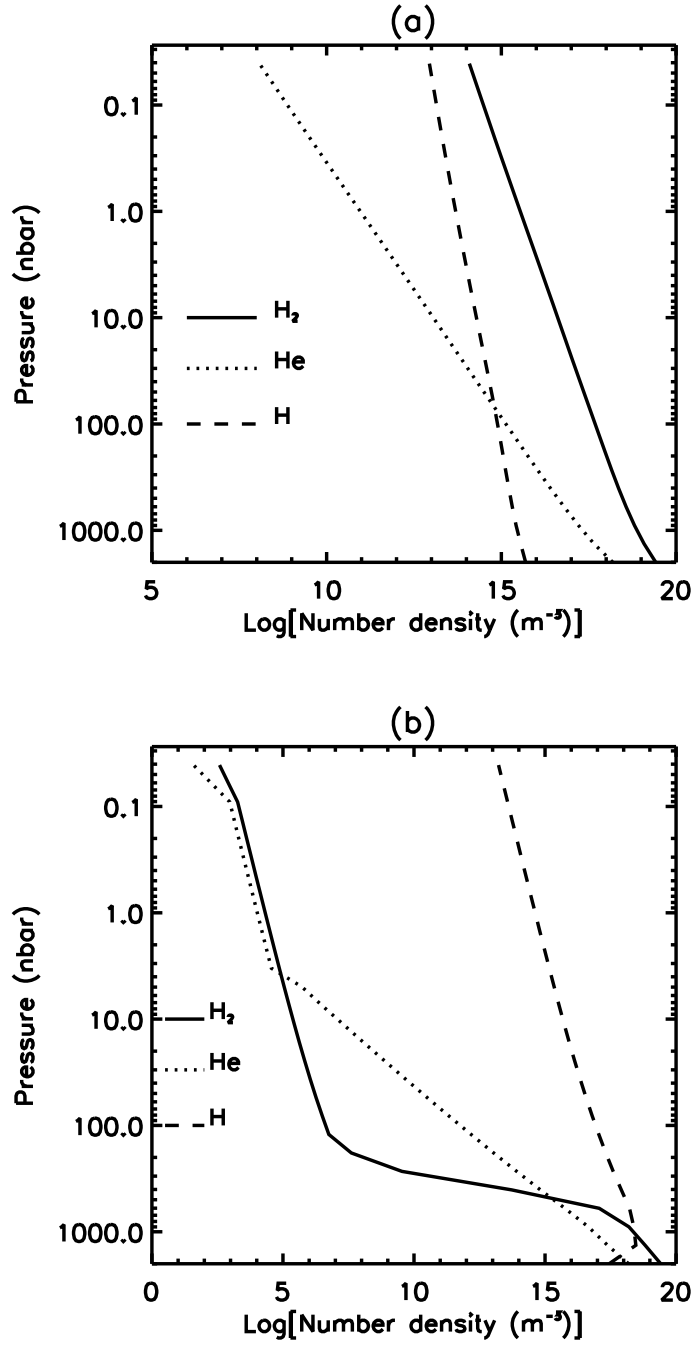


Fig. 15.— Substellar neutral number densities during apastron for (a) Exo-1, and (b) Exo-2.

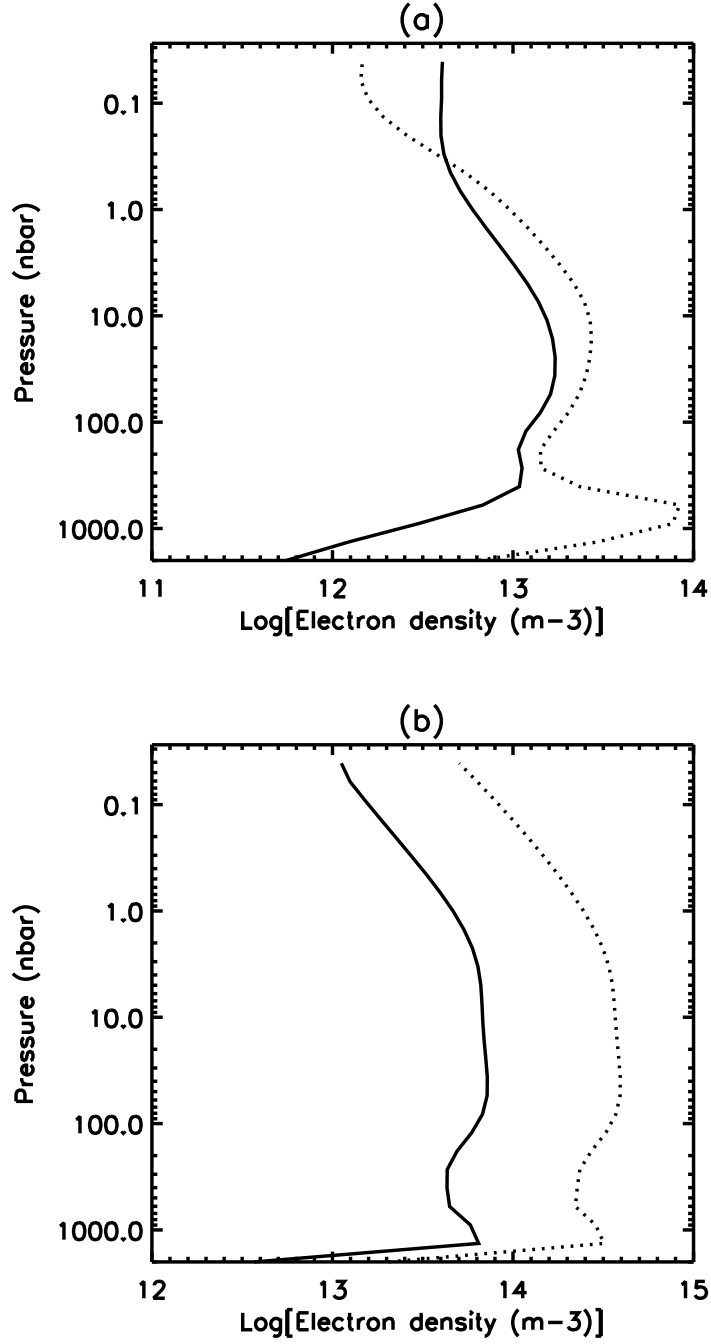


Fig. 16.— Substellar electron density profiles for (a) Exo-1 and (b) Exo-2, during apastron (solid line) and periastron (dotted line).

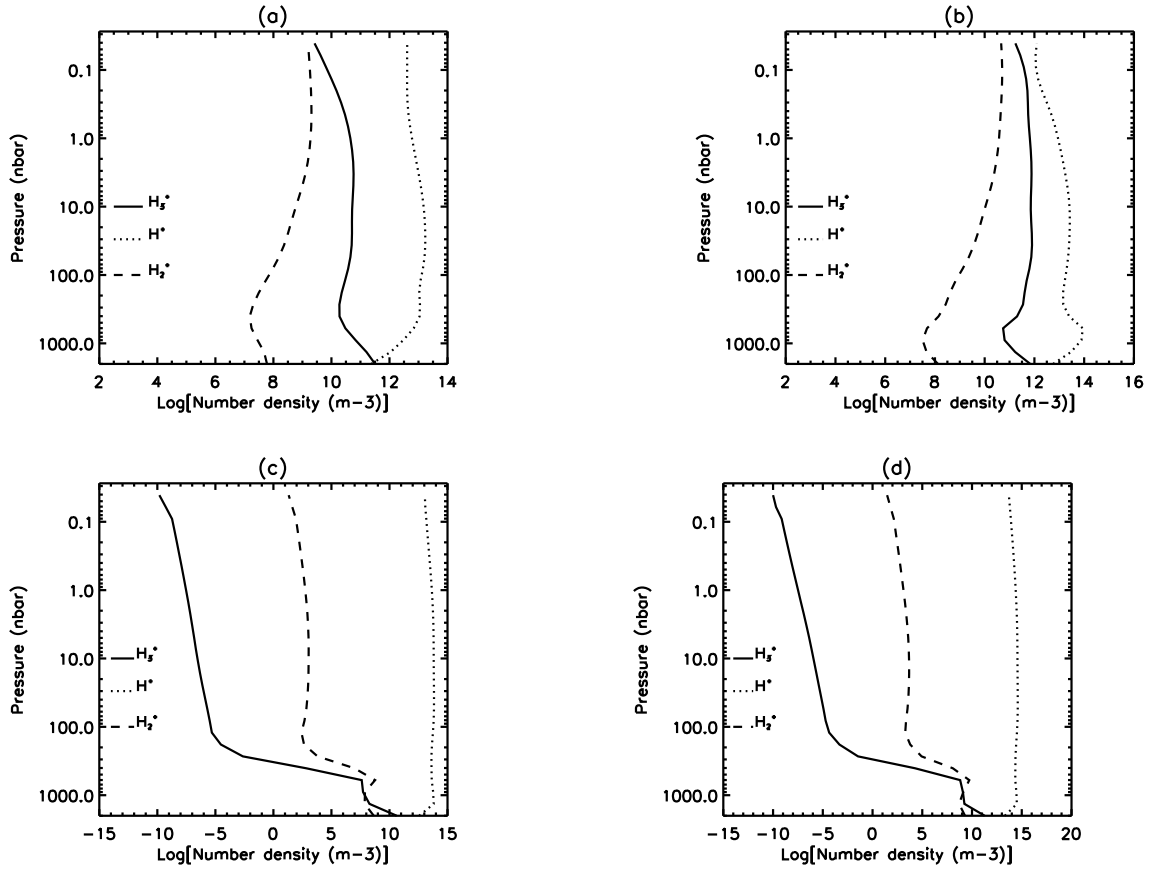


Fig. 17.— Substellar ion density profiles for Exo-1 during (a) apastron and (b) periastron, and for Exo-2 also during (c) apastron and (d) periastron.

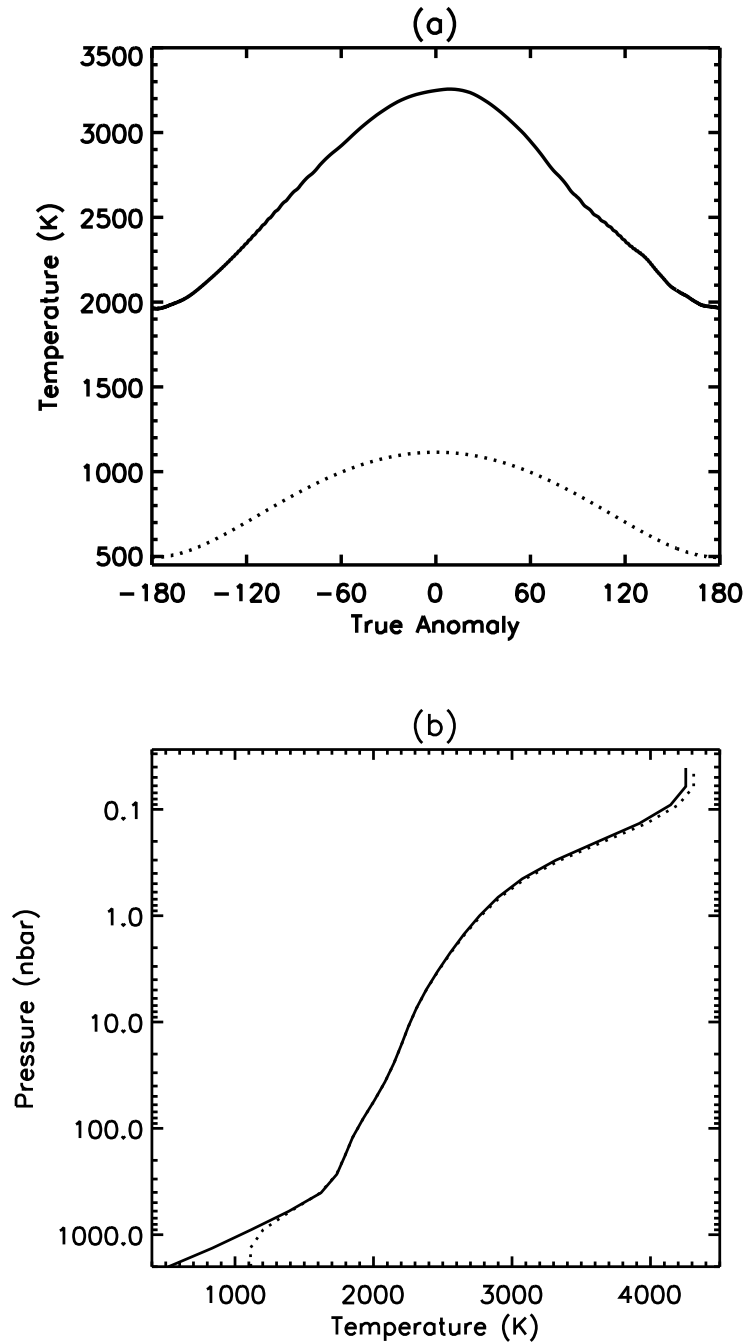


Fig. 18.— (a) Globally averaged upper boundary (at 0.04 nbar) temperature (solid line) for the simulation with a variable lower boundary temperature (Exo-3), and the equilibrium temperature of a gas giant with a Bond albedo of 0.3 (dotted line). (b) Substellar P-T profiles for the Exo-1 (solid line) and Exo-3 (dotted line) simulations at periastron.